Implementation and evaluation of the GEOS-Chem chemistry module version 13.1.2 within the Community Earth System Model v2.1

Thibaud M. Fritz[1], Sebastian D. Eastham[1,2]*, Louisa K. Emmons[3], Haipeng Lin[4], Elizabeth W. Lundgren[4], Steve Goldhaber[3], Steven R. H. Barrett[1,2], Daniel J. Jacob[4]

[1]Laboratory for Aviation and the Environment, Department of Aeronautics and Astronautics, Massachusetts Institute of Technology, Cambridge, MA 02139, USA

[2]Joint Program on the Science and Policy of Global Change, Massachusetts Institute of Technology, Cambridge, MA 02139, USA

[3]Atmospheric Chemistry Observations and Modeling Laboratory, National Center for Atmospheric Research, Boulder, CO, USA

[4]John A. Paulson School of Engineering and Applied Sciences, Harvard University, Cambridge, MA 02138, USA

*Correspondence to: Sebastian D. Eastham (seastham@mit.edu)

Short summary. We bring the state-of-the-science chemistry module GEOS-Chem into the Community Earth System Model (CESM). We show that some known differences between results from GEOS-Chem and CESM's CAM-chem chemistry module may be due to the configuration of model meteorology rather than inherent differences in the model chemistry. This is a significant step towards a truly modular ESM and allows two strong but currently separate research communities to benefit from each other's advances.

Abstract. We implement the GEOS-Chem chemistry module as a chemical mechanism in the Community Earth System Model version 2 (CESM). Our implementation allows the state-of-the-science GEOS-Chem chemistry module to be used with identical emissions, meteorology, and climate feedbacks as the CAM-chem chemistry module within CESM. We use coupling interfaces to allow GEOS-Chem to operate almost unchanged within CESM. Aerosols are converted at each time step between the GEOS-Chem bulk representation and the size-resolved representation of CESM's Modal Aerosol Model (MAM4). Land type information needed for dry deposition calculations in GEOS-Chem is communicated through a coupler, allowing online land-atmosphere interactions. Wet scavenging in GEOS-Chem is replaced with the Neu and Prather scheme, and a common emissions approach is developed for both CAM-chem and GEOS-Chem in CESM.

We compare how GEOS-Chem embedded in CESM (C-GC) compares to the existing CAM-chem chemistry option (C-CC) when used to simulate atmospheric chemistry in 2016, with identical meteorology and emissions. We compare atmospheric composition and deposition tendencies between the two simulations and evaluate the residual differences between C-GC compared to its use as a standalone chemistry transport model (S-GC). We find that stratospheric ozone agrees well between the three models with differences of less than 10% in the core of the ozone layer, but that ozone at lower altitudes is generally lower in C-GC than in either C-CC or S-GC due to greater tropospheric concentrations of bromine. This difference is not

33   uniform, with C-GC ozone 30% lower in the southern hemisphere than in S-GC but within 10% in the northern hemisphere,

34   suggesting differences in the effects of anthropogenic emissions. Aerosol concentrations in C-GC agree with those in S-GC at

35   low altitudes in the tropics but are over 100% greater in the upper troposphere due to differences in the representation of

36   convective scavenging. We also find that water vapor concentrations vary substantially between the standalone and CESM-

37   implemented version of GEOS-Chem, as the simulated hydrological cycle in CESM diverges from that represented in the

38   source MERRA-2 meteorology.

39

40   Our implementation of GEOS-Chem as a chemistry option in CESM (including full chemistry-climate feedbacks) is publicly

41   available and is being considered for inclusion in the CESM main code repository. This work is a significant step in the MUlti-

42   Scale Infrastructure for Chemistry and Aerosols (MUSICA) project, enabling two communities of atmospheric researchers

43   (CESM and GEOS-Chem) to share expertise through a common modeling framework and thereby accelerate progress in

44   atmospheric science.

45   **1   Introduction**

46   Accurate representation and understanding of atmospheric chemistry in global Earth System Models (ESMs) has been

47   recognized as an urgent priority in geoscientific model development. The National Research Council (NRC) report on a

48   National Strategy for Advancing Climate Modeling (Bretherton et al., 2012) stresses the need for including comprehensive

49   atmospheric chemistry in the next generation of ESMs. The NRC report on the Future of Atmospheric Chemistry (NRC, 2016)

50   identifies the integration of atmospheric chemistry into weather and climate models as one of its five priority science areas.

51   This work responds to those needs, presenting the implementation of the state-of-science model GEOS-Chem as an

52   atmospheric chemistry module within the Community Earth System Model (CESM).

53

54   GEOS-Chem is a state-of-the-science global atmospheric chemistry model developed and used by over 150 research groups

55   worldwide (http://geos-chem.org). It has wide appeal among atmospheric chemists because it is a comprehensive, state-of-

56   science, open-access, well-documented modeling resource that is easy to use and modify but also has strong central

57   management, version control, and user support. The model is managed at Harvard by a GEOS-Chem Support Team with

58   oversight from an international GEOS-Chem Steering Committee. Documentation and communication with users is done

59   through extensive web and wiki pages, email lists, newsletters, and benchmarking. Grass-roots model development is done by

60   users, and inclusion into the standard model is prioritized by Working Groups reporting to the Steering Committee. The model

61   can simulate tropospheric and stratospheric oxidant-aerosol chemistry, aerosol microphysics, and budgets of various gases .

62   Simulations can be conducted on a wide range of computing platforms with either shared-memory (OpenMP) or distributed

63   memory (MPI) parallelization – with this latter implementation referred to as GEOS-Chem High Performance, or GCHP

64   (Eastham et al., 2018).

65

66 For the general atmospheric chemistry problem involving K atmospheric species coupled by chemistry and/or aerosol
67 microphysics, GEOS-Chem solves the system of K coupled continuity equations

68

69
$$\frac{\partial n_i}{\partial t} = -\nabla \cdot (n_i \mathbf{U}) + P_i(\mathbf{n}) - L_i(\mathbf{n}) \qquad (1)$$
70

71 where $\mathbf{n} = (n_1, \ldots n_K)^T$ is the number density vector representing the concentrations of the K species, $\mathbf{U}$ is the 3-D wind vector,
72 and P_i and L_i are local production and loss terms for species i including emissions, deposition, chemistry, and aerosol physics.
73 The transport term $-\nabla \cdot (n_i \mathbf{U})$ includes advection by grid-resolved winds as well as parameterized subgrid turbulent motions
74 (boundary layer mixing, convection). The local term $P_i(\mathbf{n})$ $–L_i(\mathbf{n})$ couples the continuity equations across species through
75 chemical kinetics and aerosol physics.

76

77 Standard application of the GEOS-Chem model as originally described by Bey et al. (2001) is off-line, meaning that the model
78 does not simulate its own atmospheric dynamics. Instead, it uses winds and other meteorological variables archived from the
79 Goddard Earth Observation System (GEOS) of the NASA Global Modeling and Assimilation Office (GMAO). These archives
80 are produced by GEOS ESM simulations with assimilated meteorological observations, currently at a horizontal resolution of
81 0.25°×0.3125°. GEOS-Chem simulations can be conducted at that native resolution or at coarser resolution (by conservative
82 re-gridding of meteorological fields). Long et al. (2015) developed an on-line capability for GEOS-Chem to be used as a
83 chemical module in ESMs, with initial application to the GEOS ESM. In that configuration, GEOS-Chem only solves the
84 local terms of the continuity equation

85

86
$$\frac{\partial n_i}{\partial t} = P_i(\mathbf{n}) - L_i(\mathbf{n}) \qquad (2)$$
87

88 and delivers the updated concentrations to the ESM for computation of transport through its atmospheric dynamics. On-line
89 simulation avoids the need for a meteorological data archive and the associated model transport errors (Jöckel et al., 2001; Yu
90 et al., 2018). It also enables fast coupling between chemistry and dynamics.

91

92 Transformation of GEOS-Chem to a grid-independent structure was performed transparently, such that the standard GEOS-
93 Chem model uses the exact same code for on-line and off-line applications. This includes a mature implementation within the
94 GEOS ESM. It was applied recently to a year-long tropospheric chemistry simulation with ≈12 km (cubed-sphere c720) global
95 resolution, and is now being used for global air quality forecasting and chemical data assimilation (Keller et al., 2017; Hu et
96 al., 2018; Keller et al., 2021). However, the only implementations of GEOS-Chem which are currently publicly available are
97 either designed to run "offline", driven by archived meteorological data from the NASA Goddard Earth Observing System

98   (GEOS) (Bey et al., 2001; Eastham et al., 2018), or operate at regional scale and do not extend to global simulation (Lin et al.,

99   2020; Feng et al., 2021).

100

101   Integration of GEOS-Chem as a chemistry option within an open-access, global ESM responds to the aforementioned calls

102   from the NRC. One of the most widely used open-access ESM is the Community Earth System Model (CESM) (Hurrell et al.,

103   2013). CESM is fully coupled and state-of-science. It produces its own meteorology based on fixed sea surface temperatures

104   or with a fully interactive ocean model. It can also be nudged to observed meteorology including from GEOS. The CESM

105   configuration with chemistry covering the troposphere and stratosphere is referred to as CAM-chem (Community Atmosphere

106   Model with chemistry) (Tilmes et al., 2016; Lamarque et al., 2012). CAM-chem is a state-of-science model of atmospheric

107   chemistry; it has participated (along with CESM's WACCM model which extends to the lower thermosphere) in many

108   international model intercomparison activities such as ACCMIP, CCMI, POLMIP, HTAP2, GeoMIP and CMIP6, and has a

109   large international user community. CAM-chem also has a very different development heritage from GEOS-Chem, with each

110   model providing better performance in comparison to observations in different areas (Park et al., 2021; Emmons et al., 2015;

111   Nicely et al., 2017; Jonson et al., 2018). The fundamental differences in implementation of almost every atmospheric process

112   between GEOS-Chem and CAM-chem mean that it is difficult to disentangle the root causes of these differences.

113

114   Modular Earth system models can resolve this issue. Allowing individual scientific components to be swapped freely allows

115   researchers to evaluate exactly what effect that component has in isolation, while also giving a single user base access to a

116   larger portfolio of options. If two different models each implement five processes in different ways, a researcher must learn to

117   use both in order to compare their results and cannot isolate the effect of any one process with confidence. If process options

118   are implemented in the same framework, this problem is avoided. Such modularity is becoming increasingly possible with the

119   availability of Earth system infrastructure such as the Earth System Modeling Framework (ESMF) and the National Unified

120   Operational Prediction Capability (NUOPC), which describe common interfaces for Earth system modeling components (Hill

121   et al., 2004; Sandgathe et al., 2011). The Multi-Scale Infrastructure for Chemistry and Aerosols (MUSICA) builds upon this

122   trend with process-level modularization, with the goal of allowing researchers to select from a range of community-developed

123   options when performing atmospheric simulations.

124

125   This work integrates the GEOS-Chem chemistry module into CESM as an alternative option to CAM-chem. Our

126   implementation allows researchers to select either model to simulate gas-phase and aerosol chemistry throughout the

127   troposphere and stratosphere, while other processes such as advection, broadband radiative transfer, convective transport, and

128   emissions are handled nearly identically. We demonstrate this capability by comparing simulations of the year 2016 as

129   generated by GEOS-Chem and CAM-chem operating within CESM, with the chemical module being the only difference.

130   Estimates of atmospheric composition are compared between the two models and against a simulation in the standalone GEOS-

131 Chem High Performance (GCHP) chemistry transport model (CTM). Finally, we evaluate the accuracy of the three approaches

132 against observations of atmospheric composition and deposition.

133

134 Section 2 provides a technical description of the implementation of GEOS-Chem into CESM. Section 3 then describes a two-

135 year simulation performed in CESM with GEOS-Chem; CESM with CAM-chem; and the standalone GEOS-Chem CTM. This

136 includes model setup (Section 3.1), intercomparison (Section 3.2), and evaluation against surface and satellite measurements

137 (Section 3.3).

## 2   Coupling between GEOS-Chem and CESM

139 We first describe the interface used within CESM when using either the CAM-chem or GEOS-Chem options (Section 2.1).

140 Unless otherwise stated, "GEOS-Chem" refers to the grid independent chemistry module which is common to all

141 implementations, including standalone GEOS-Chem with OpenMP (Classic) or MPI (GCHP) parallelization, NASA GMAO's

142 GEOS ESM, and WRF-GC. We then briefly summarize the chemistry and processes represented by the CAM-chem and

143 GEOS-Chem options within CESM (Section 2.2). This is followed by a description of differences between the implementation

144 of GEOS-Chem in CESM and its stand-alone code (Section 2.3), differences in the data flow through CESM when using

145 GEOS-Chem as opposed to CAM-chem (Section 2.4), and finally the installation and compilation process (Section 2.5).

2.1   Interface

147 Our approach embeds a full copy of the GEOS-Chem chemistry module source code (version 13.1.2) within CESM (version

148 2.1.1). All modifications made to the GEOS-Chem source code have been propagated to the GEOS-Chem main code branch

149 (https://github.com/geoschem/geos-chem) to ensure future compatibility between CESM and GEOS-Chem. Information is

150 passed between the CESM Community Atmosphere Model (CAM) version 6 (CAM6) and the GEOS-Chem routines through

151 an interface layer developed as part of this work. A schematic representation of the implementation is provided in Figure 1.

152
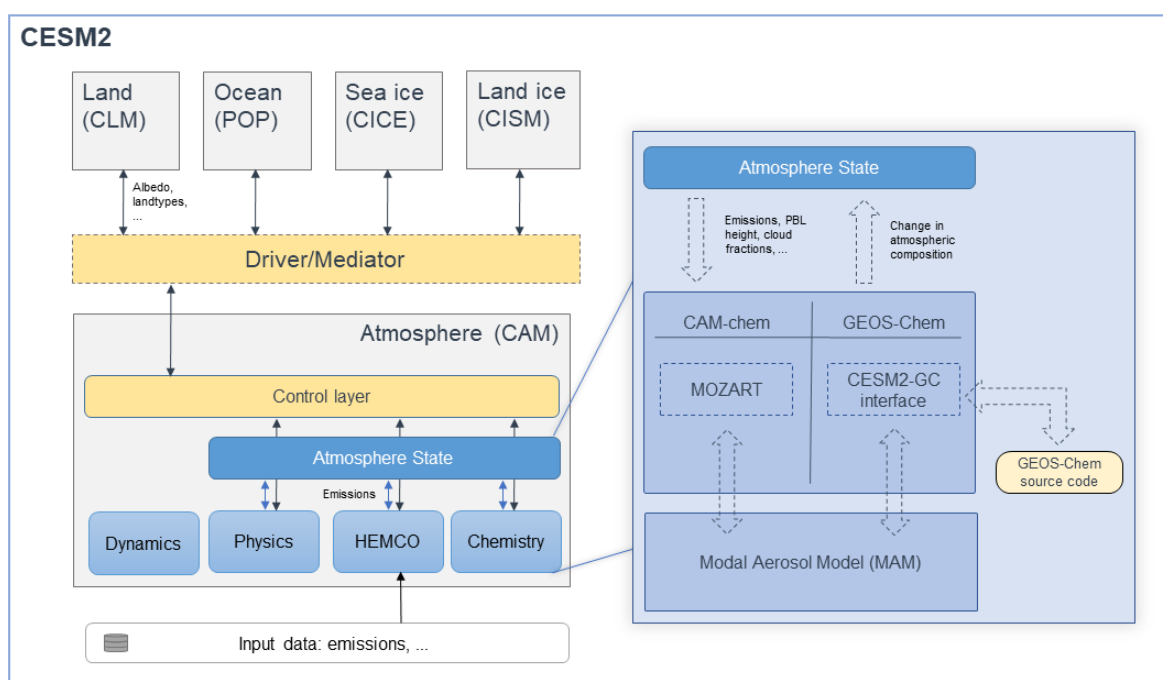
153

154 *Figure 1. Architectural overview of CESM when running with either the GEOS-Chem or CAM-chem chemistry options. The left section*
155 *shows the architecture of CESM, where the five major Earth system components are connected through the driver/mediator. The work*
156 *presented here changes only the contents of the atmosphere component (CAM). Regardless of the chemistry option used, dynamics,*
157 *physics, and emissions (HEMCO) are handled identically. Each component modifies the "Atmosphere State" while communication occurs*
158 *through the control layer. The choice of chemistry module is confined to the "Chemistry" subcomponent, where either CAM-chem or*
159 *GEOS-Chem can be chosen. In each case, data are transmitted between the "Atmosphere State" and the chemistry module, which*
160 *interacts in turn with the Modal Aerosol Model.*

161 At each time step, CESM calls the coupling interface which fills in the meteorological variables required by either CAM-chem
162 or GEOS-Chem. Atmospheric transport and physics are identical whether using CAM-chem or GEOS-Chem to simulate
163 atmospheric chemistry. The interface passes species concentrations from CAM to GEOS-Chem, which are then modified by
164 GEOS-Chem and passed back to CAM. Meteorological data and land data are also passed to GEOS-Chem through the same
165 interface. The routine calls in CAM when using either GEOS-Chem or CAM-chem are identical, with the appropriate chemistry
166 module defined at compilation time such that the calls are routed to the appropriate routines.

167

168 The interface handles the conversion of meteorological variables and concentrations of atmospheric constituents between the
169 state variables in CAM and those used in GEOS-Chem. Since GEOS-Chem operates in a "grid-independent" fashion, changes
170 in the grid specification and other upstream modifications to CESM do not necessitate any changes to this interface (Long et
171 al., 2015). Our version of CESM 2.1.1 is modified such that emissions are handled by the Harmonized Emissions Component
172 (HEMCO), which operates independently of the chemistry module and can provide emissions data to either CAM-chem or
173 GEOS-Chem equally (Lin et al., 2021).

6

174

175 The interface code is kept in the `src/chemistry/geoschem` subfolder, which also contains a copy of the source code for

176 GEOS-Chem. Unlike the implementation of GEOS-Chem within GEOS, we do not use ESMF. However, we plan to develop

177 a NUOPC-based interface as part of future work.

2.2 Processes represented by CAM-chem and GEOS-Chem

179 CAM-chem uses the Model for OZone And Related chemical Tracers (MOZART) family of chemical mechanisms to simulate

180 atmospheric chemistry (Emmons et al., 2020). The tropospheric-stratospheric MOZART-TS1 scheme which we demonstrate

181 in our intercomparison involves 186 gas-phase chemical species and includes stratospheric bromine, chlorine, and fluorine

182 chemistry. MOZART-TS1 does not include detailed tropospheric halogen chemistry or short-lived halogen sources such as

183 sea salt bromine, although these will be available in a future release (Badia et al., 2021; Fernandez et al., 2021). Photolysis

184 rates are calculated using a lookup table, based on calculations with the Tropospheric Ultraviolet and Visible (TUV) radiation

185 model (Kinnison et al., 2007). Wet deposition is calculated using the Neu and Prather (2012) scheme for both convective and

186 large-scale precipitation. Dry deposition velocities over land are calculated for each land type by the Community Land Model

187 (CLM) in CESM using the Wesely (1989) resistance scheme with updates described by Emmons et al. (2020). Deposition

188 velocities over the ocean are calculated separately in CAM-chem. Aerosols are represented using the 4-mode Modal Aerosol

189 Model (MAM4), which includes sulfate, black carbon, primary, and secondary organic aerosols (Mills et al., 2016).

190 Ammonium and ammonium nitrate aerosols are calculated with a parameterization using the bulk aerosol scheme (Tilmes et

191 al., 2016). Secondary organic aerosols are simulated using a 5-bin volatility basis set (VBS) scheme, formed from terpenes,

192 isoprene, specific aromatics and lumped alkanes through reaction with OH, O_3 and NO_3, with unique yields for each reach and

193 bin (Tilmes et al., 2019). This more detailed scheme differs from the default MAM SOA scheme that is used in CAM6 (without

194 interactive chemistry). Aerosol deposition, including dry and wet deposition, and gravitational settling (throughout the

195 atmosphere) are calculated in the MAM code of CESM. CAM-chem also uses a volatility basis set (VBS) approach for SOA

196 with five volatility bins, covering saturation concentrations with logarithmic spacing from 0.01 to 100 $\mu g/m^3$. CAM-chem

197 explicitly represents Aitken and accumulation mode SOA using two separate tracers for each volatility bin but does not include

198 an explicit representation of non-volatile aerosol.

199

200 GEOS-Chem uses a set of chemical mechanisms implemented with the Kinetic PreProcessor (KPP) (Damian et al., 2002). The

201 standard chemical mechanism has evolved continuously from the tropospheric gas-phase scheme described by Bey et al. (2001)

202 and now includes aerosol chemistry (Park, 2004), stratospheric chemistry (Eastham et al., 2014), and a sophisticated

203 tropospheric-stratospheric halogen chemistry scheme (Wang et al., 2019). The scheme present in GEOS-Chem 13.1.2 includes

204 299 chemical species. Additional "specialty simulations" such as an aerosol-only option and a simulation of the global mercury

205 cycle are present in GEOS-Chem but are not implemented into CESM in this work. Photolysis rates are calculated using the

206 Fast-JX v7 model (Wild et al., 2000; Fast-JX v7.0a). When implemented standalone, wet deposition is calculated for large-

207 scale precipitation using separate approaches for water-soluble aerosols (Liu et al., 2001) and gases (Amos et al., 2012) with

208 calculation of convective scavenging performed inline with convective transport. A different approach is used to simulate wet

209 scavenging for the implementation of GEOS-Chem in CESM (see Section 2.3.4). Dry deposition is calculated using the Wesely

210 (1989) scheme (Wang et al., 1998), but with updates for HNO_3 (Jaeglé et al., 2018), aerosols (Jaeglé et al., 2011; Alexander

211 et al., 2005; Fairlie et al., 2007; Zhang et al., 2001), and over ocean (Pound et al., 2020). The representation of aerosols in

212 GEOS-Chem varies by species. Sulfate-ammonium-nitrate aerosol is represented using a bulk scheme (Park, 2004), with gas-

213 particle partitioning determined using ISORROPIA II (Fountoukis and Nenes, 2007). Modal and sectional size-resolved

214 aerosol schemes are available for GEOS-Chem (Kodros and Pierce, 2017; Yu and Luo, 2009), but are disabled by default and

215 not used in this work. Sea salt aerosol is represented using two (fine and coarse) modes (Jaeglé et al., 2011), while dust is

216 represented using four size bins (Fairlie et al., 2007). We use the "complex SOA" chemistry mechanism in GEOS-Chem when

217 running in CESM, as this uses a volatility basis set (VBS) representation of secondary organic aerosol which is broadly

218 compatible with that used in CAM-chem (Pye and Seinfeld, 2010; Marais et al., 2016; Pye et al., 2010). The complex SOA

219 VBS scheme uses four volatility bins covering saturation concentrations on a logarithmic scale from 0.1 to 100 $\mu g/m^3$. Two

220 classes of SOA are represented in this fashion: those derived from terpenes (TSOA) and those derived from aromatics (ASOA).

221 For each "class" of SOA, two tracers are used to represent each volatility bin (one holding the gas phase mass, the other holding

222 the condensed phase mass). The only exception is the lowest-volatility aromatic aerosol, which is considered to be non-volatile

223 and therefore has no gas-phase tracer. Two additional SOA tracers, representing isoprene-derived and glyoxal-derived SOA,

224 are not represented using a VBS approach.

225

226 Additional differences between the two chemistry modules include the use of different Henry's law coefficients, gravitational

227 settling schemes, representation of polar stratospheric clouds, and heterogeneous chemistry. Full descriptions of the two

228 models are available at https://geos-chem.seas.harvard.edu/narrative and in Emmons et al. (2020).

229 **2.3   Representation of atmospheric processes in GEOS-Chem when running in CESM**

230 Some processes cannot be easily transferred from standalone GEOS-Chem to its implementation in CESM, due to factors such

231 as the different splitting of convective transport in the two models. Processes which vary in their implementation between the

232 standalone and CESM implementations of GEOS-Chem are described below.

233 **2.3.1   Aerosol coupling in CESM with GEOS-Chem**

234 Since GEOS-Chem and CESM use different approaches to represent aerosols, there is no straight-forward translation between

235 the GEOS-Chem representation and that used elsewhere in CESM. We implement an interface between the CESM and GEOS-

236 Chem representations, so that GEOS-Chem's processing of aerosols is most accurately represented without compromising the

237 microphysical simulations and radiative interactions of aerosol calculated elsewhere in CESM.

238

239   CESM uses the 4-mode version of the Modal Aerosol Model (MAM4) to represent the aerosol size distribution and perform

240   aerosol microphysics (Liu et al., 2016). This represents the mass of sulfate aerosols, secondary organic matter (in five volatility

241   basis set bins), primary organic matter, black carbon, soil dust, and sea salt with advected tracers for each mode (accumulation,

242   Aitken, coarse, and primary carbon), although some species are considered only in a subset of the four modes. A tracer is also

243   implemented for the number of aerosol particles in each mode, resulting in a total of 18 tracers. As discussed above, GEOS-

244   Chem instead represents sulfate, nitrate, and ammonium aerosol constituents with three tracers; fresh and aged black and

245   organic carbon with four tracers; fine and coarse sea salt as two tracers; and different sizes of dust with four tracers. Six

246   additional tracers are used to track the bromine, iodine, and chlorine content of each mode of sea salt aerosol, with two more

247   used to track overall alkalinity. Gas-phase sulfuric acid is assumed to be negligible in the troposphere and is estimated using

248   an equilibrium calculation in the stratosphere (Eastham et al., 2014). The GEOS-Chem mechanism therefore represents greater

249   chemical complexity but reduced size resolution compared to the aerosol representation in MAM4.

250

251   Accordingly, when receiving species concentrations from CESM, the interface to GEOS-Chem lumps all modes of the MAM

252   aerosol into the corresponding GEOS-Chem tracer. This includes gas-phase H_2SO_4, in the case of the GEOS-Chem sulfate

253   (SO4) tracer. Aerosol constituents which are not represented explicitly by MAM (e.g. nitrates) are not included in this

254   calculation. The relative contribution of each mode is stored during this "lumping" process for each grid cell. Once calculations

255   with GEOS-Chem are complete, the updated concentration of the lumped aerosol is repartitioned into the MAM tracers based

256   on the stored relative contributions in each grid cell.

257

258   For secondary organic aerosols (SOA), additional steps are needed. For the bins covering saturation concentrations of 1 µg/m^3

259   and greater, we assume that the relevant volatility bin in MAM4 is equal to the sum of the two classes in GEOS-Chem covering

260   the same saturation concentrations. For example, the tracers TSOA1 and ASOA1 in GEOS-Chem are combined to estimate

261   the total quantity of the Aitken and accumulation modes for species "soa3" in MAM4. Partitioning between the two modes

262   (when transferring from GEOS-Chem to MAM4) is calculated based on the relative contribution of each constituent to the

263   total prior to processing by GEOS-Chem. Partitioning between the two classes (when transferring from MAM4 to GEOS-

264   Chem) is calculated based on the relative contribution of each constituent to the total at the end of the previous time step. For

265   the lowest-volatility species, we split the lowest volatility bin concentrations (and non-volatile species) from GEOS-Chem

266   between the two lowest volatilities in MAM4. A full mapping for all species is provided in Table 1.

267

268   *Table 1. Mapping between tracers used to represent SOA in GEOS-Chem and CAM-chem (CESM). Translation between GEOS-Chem and*
269   *MAM4 is performed by preserving the relative contributions provided during the previous transfer.*

GEOS-Chem species	Mapping to CAM-chem species	Saturation concentration range (µg/m^3)	Phase
TSOA0 + ASOAN	soa1_a1 + soa1_a2 + soa2_a1 + soa2_a2	0 – 0.1	Aerosol
TSOA1 + ASOA1	soa3_a1 + soa3_a2	0.1 – 1.0	Aerosol

TSOA2 + ASOA2	soa4_a1 + soa4_a2	1.0 – 10	Aerosol
TSOA3 + ASOA3	soa5_a1 + soa5_a2	10 – 100	Aerosol
TSOG0	SOAG0 + SOAG1	0 – 0.1	Gas
TSOG1 + ASOG1	SOAG2	0.1 – 1.0	Gas
TSOG2 + ASOG2	SOAG3	1.0 – 10	Gas
TSOG3 + ASOG3	SOAG4	10 – 100	Gas

270

271 Finally, MAM simulates some chemical processing on and in the aerosol. This includes the reaction of sulfur dioxide with

272 hydrogen peroxide and ozone in clouds, which is already included in the GEOS-Chem chemistry mechanism. We therefore

273 disable in-cloud sulfur oxidation in MAM4 when using the GEOS-Chem chemistry component in CESM, consistent with the

274 GEOS-Chem CTM. A comparison of the effect of each approach is provided in the Supplementary Information.

275 **2.3.2 Dry deposition**

276 Dry deposition velocities over land are calculated in CESM for each atmospheric constituent by the Community Land Model

277 (CLM) using a species database stored by the coupler. GEOS-Chem is also able to calculate its own dry deposition velocities

278 (see Section 2.2), in situations where a land model is not available such as when running as a CTM. We thus implement

279 different options to compute dry deposition velocities when running CESM with the GEOS-Chem chemistry option:

280   1. Dry deposition velocities over land are computed by CLM and are passed to CAM through the coupler. They are then

281   merged with dry deposition velocities computed over ocean and ice by GEOS-Chem, identical to the procedure used

282   in CAM-chem. Each of these are scaled by the land and ocean/ice fraction respectively.

283   2. GEOS-Chem computes dry deposition at any location using the land types and leaf area indices from CLM, which

284   are passed through the coupler.

285   3. GEOS-Chem obtains "offline" land types and leaf area indices and computes the dry deposition velocities similarly

286   to GEOS-Chem Classic.

287 This allows researchers to experiment with different dry deposition options, ranging from that most consistent with the

288 approach used in CAM-chem (option 1) to that most consistent with stand-alone GEOS-Chem (option 3). For this work we

289 use option 2, but option 1 will be brought as standard into the CESM main code to reduce data transfer requirements.

290 **2.3.3 Emissions**

291 The Harmonized Emissions Component (HEMCO) is used to calculate emissions in standalone GEOS-Chem (Keller et al.,

292 2014), and HEMCO v3.0 was recently implemented as an option for CAM-chem (Lin et al., 2021). HEMCO offers the

293 possibility for the user to read, regrid, overlay, and scale emission fluxes from different archived emissions inventories at

294 runtime. Emissions extensions allow for the computation of emissions that depend on meteorology or surface characteristics

295 (e.g. lightning, dust emissions). Some extensions have also been designed to calculate subgrid-scale chemical processes, such

296 as non-linear chemistry in ship plumes (Vinken et al., 2011).

297

298 The GEOS-Chem CTM implementations use archived ("offline") inventories of natural emissions, calculated at native

299 resolution using the NASA GEOS MERRA-2 and GEOS-FP meteorological fields. This ensures that the emissions are

300 calculated consistently regardless of grid resolution. These archived emissions fields can be used within CESM but we also

301 preserve the option for users to employ "online" emissions inventories where relevant. This enables feedbacks between climate

302 and emissions to be calculated. For instance, lightning NO_x emissions, dust and sea salt emissions, and biogenic emissions are

303 all computed online using parameterizations from CAM and CLM. CAM computes lightning NO_x emissions based on the

304 lightning flash frequency, which is estimated following the model cloud height, with different parameterizations over ocean

305 and land. The NO lightning production rate in CAM is assumed proportional to the discharged energy, with 10^{17} atoms of

306 nitrogen released per Joule (Price et al., 1997). The lightning NO_x emissions are then allocated vertically from the surface to

307 the local cloud top based on the distribution described by Pickering et al. (1998). For biogenic emissions, we use the online

308 Model of Emissions of Gases and Aerosols from Nature version 2.1 (MEGANv2.1), as established in CLM (Guenther et al.,

309 2012). Aerosol mass and number emissions are passed directly to MAM constituents. Global anthropogenic emissions can be

310 specified from any of the standard GEOS-Chem inventories, but default to the Community Emissions Data System (CEDS)

311 inventory (Hoesly et al., 2018). Sulfur emissions from the CEDS inventory are partitioned into size-resolved aerosol (mass

312 and number) and SO_2 (Emmons et al., 2020). In CAM, volcanic out-gassing of SO_2 is provided from the GEIA inventory with

313 2.5% emitted as sulfate aerosol (Andres and Kasgnoc, 1998), while eruptive emissions are provided from the VolcanEESM

314 database (Neely and Schmidt, 2016). The option is also available through HEMCO to use the "AeroCom" volcanic emissions,

315 which are derived from OMI observations of SO_2 (Ge et al., 2016; Carn et al., 2015).

316

317 Although we use HEMCO with both model configurations, there remain differences between the representation of emissions

318 in CAM-chem and in GEOS-Chem when run within CESM. This is because of differences in the species present in their

319 respective mechanisms. For instance, emissions of iodocarbons (CH_3I, CH_2I_2, CH_2ICl, CH_2IBr) and inorganic iodine (HOI, I_2)

320 are not available in CAM-chem since iodine is not explicitly modeled in CESM v2.1.1. VOC lumping is also performed

321 differently (see the Supplemental Information for more detail).

322

323 Where the emitted species are present in both chemical mechanisms, the emissions calculated by HEMCO in CESM are

324 identical whether running with either GEOS-Chem and CAM-chem. If the HEMCO implementations of lightning, dust, sea

325 salt, and biogenic emissions are used, emissions will be identical between CESM and the standalone GEOS-Chem CTM.

326 **2.3.4   Wet deposition and convection**

327 For both GEOS-Chem and CAM-chem within CESM, convective scavenging and transport are handled separately. Wet

328 deposition is performed using the Neu scheme (Neu and Prather, 2012), which simulates uptake and removal of soluble species

329 by large-scale and convective precipitation. Unlike in the Liu et al. (2001) approach implemented in the GEOS-Chem

11

330 standalone code, removal of soluble gases within convective updrafts is not explicitly simulated in either CAM-chem or GEOS-

331 Chem when embedded in CESM. When using the CAM-chem mechanism within CESM, the Neu scheme is used to perform

332 washout of soluble gaseous species, while wet deposition of MAM aerosols is handled by MAM. When running CESM with

333 the GEOS-Chem chemistry mechanism, the Neu scheme also performs wet scavenging for aerosols which are not represented

334 by MAM4 (e.g. nitrate). For all such aerosols we assume a Henry's law coefficient equal to that for HNO_3.

2.3.5   Surface boundary conditions

336 In CESM, surface boundary mixing ratios of long-lived greenhouse gases (methane, N_2O, and chlorofluorocarbons) are set to

337 the fields specified for CMIP6 historical conditions and future scenarios (Meinshausen et al. 2017). For whichever scenario is

338 chosen, the boundary conditions overwrite those set by the GEOS-Chem chemistry module or by the HEMCO emissions

339 component.

2.4   Changes to the data flow in CESM when running with GEOS-Chem

341 In CESM, data such as the Henry's law coefficients required to calculate dry deposition velocities and wet scavenging rates

342 for each species are defined at compile time. For species that are common to GEOS-Chem and CAM-chem but where these

343 factors differ, the GEOS-chem values are used by default. The CAM-Chem values are listed alongside them in the source code

344 to allow users to switch if desired. Additionally, we modify CAM, CLM and CIME such that the land model can pass land

345 type information and leaf area indices to the atmosphere model to compute dry deposition velocities. This could be a potential

346 solution for dry deposition of aerosols in MAM, which currently uses fixed land types independent of the ones used in CLM

347 (Liu et al., 2012). However, this comes at the cost of passing land information through the coupler at every time step.

2.5   Installation and compilation process

349 The interface between CESM and GEOS-Chem, as well as the GEOS-Chem source code, is automatically downloaded when

350 CAM checks out its external repositories. The versions of GEOS-Chem and of the coupling interface can be changed by

351 modifying the `Externals_CAM.cfg` and by running the `checkout_externals` command.

352

353 When creating a new case, the user chooses the atmospheric chemistry mechanism (GEOS-Chem or CAM-chem). The

354 chemistry option is defined by the name of the CESM configuration (component set, or "compset"), making the process of

355 creating a run directory almost identical when choosing either GEOS-Chem or CAM-chem. Whereas chemistry options in

356 CAM-chem are set explicitly using namelist files, certain options in GEOS-Chem are set using ASCII text input files which

357 are read during the initialization sequence. The installation and build infrastructure of CIME will therefore copy any GEOS-

358 Chem specific text input files to the case directory when setting up a simulation which includes GEOS-Chem. This currently

359 includes emissions specifications read by HEMCO, although this is expected to change as HEMCO becomes the standard

360 emissions option for both CAM-chem and GEOS-Chem.

361

362 Although CESM supports both shared-memory parallelization (OpenMP) and distributed memory parallelization (MPI),

363 GEOS-Chem implemented in CESM does not currently support OpenMP. When running CESM with the GEOS-Chem

364 chemistry model, the number of OpenMP threads per MPI task is therefore set to one.

365

366 Although a complete copy of the GEOS-Chem source code is downloaded (to ensure , not all files present in the GEOS-Chem

367 source code directory are compiled. For instance, the files pertaining to the GEOS-Chem advection scheme are not needed as

368 advection is performed by CAM, and therefore the GEOS-Chem advection routines are not compiled. To do this we implement

369 a new feature in CIME to use `.exclude` files which list files not needed during compilation. CIME reads each `.exclude`

370 file at compile time and searches subdirectories recursively from the location of the exclude file, preventing any named file

371 from being included in compilation. For example, an `.exclude` file is provided in the chemistry coupling interface folder

372 for GEOS-Chem that lists the files to exclude in the GEOS-Chem source code directories.

373 ## 3   Model evaluation

374 We simulate a two-year period with GEOS-Chem embedded in CESM (hereafter C-GC), to support two evaluations. First, we

375 perform a comparison of its output to that generated by two other model configurations (Section 3.2). By comparing the results

376 to those produced for the same period by CESM with CAM-chem (hereafter C-CC), we can perform the first comparison of

377 GEOS-Chem and CAM-chem when run as chemistry modules within the same ESM. Any differences between these two

378 simulations can only be the result of differences between the two chemical modules and their implementations in CESM. This

379 includes not only differences in the gas-phase chemical mechanism, but also in the implementation of photolysis calculations,

380 heterogeneous chemistry, aerosol microphysics, and the chemical kinetics integrator itself. We also compare output to that

381 produced by the standalone GEOS-Chem (hereafter S-GC). This enables us to evaluate the effect of using CESM's grid

382 discretization, advection, aerosols, and representation of meteorology compared to that used in the GEOS-Chem CTM.

383

384 Second, we evaluate the performance of C-GC by comparing output to observational data (Section 3.3). We also include

385 comparisons of data from the C-CC and S-GC configurations, to provide insight into the relative performance of the model

386 and the root cause of disagreements with observations.

387 ### 3.1   Simulation setup

388 All simulations cover the period January 1ˢᵗ 2015 to December 31ˢᵗ 2016, with the first year discarded as spinup. For C-CC,

389 the standard restart file provided with CESM is used to provide initial conditions. For S-GC, we use a restart file provided with

390 version 13.1.2 of the GEOS-Chem chemistry module. For C-GC, we use initial conditions which are taken from the S-GC

391 restart file where possible, but fill missing species (e.g. MAM4 aerosol tracers) using data from the C-CC restart file. Both

392 simulations performed with CESM v2.1.1 (C-GC and C-CC) use a horizontal resolution of 1.9°×2.5° on 56 hybrid pressure

393 levels, extending from the surface to 1.65 hPa. Aerosols are represented in CESM using the 4-mode version of the modal

394 aerosol model, MAM4 (Liu et al., 2012). In C-GC, we use the complex SOA chemistry scheme (Pye and Seinfeld, 2010; Pye

395 et al., 2010; Marais et al., 2016). In C-CC, we use the MOZART-TS1 chemistry scheme (Emmons et al., 2020).

396

397 Standalone GEOS-Chem (S-GC) simulations are performed using the GEOS-Chem High Performance (GCHP) configuration,

398 using a C48 cubed-sphere grid (approximately equivalent to a 2°×2.5° horizontal grid) on 72 hybrid pressure levels extending

399 up to 1 Pa. In GCHP, chemistry is performed up to 1 hPa (~50 km) with simplified parameterizations used above that point.

400 Aerosols are represented using GEOS-Chem's "native" scheme, without translation to or from MAM4. As in C-GC, we use

401 the complex SOA scheme.

402

403 All three model configurations are driven using meteorological data from the Modern Era Retrospective analysis for Research

404 and Applications, version 2 (MERRA-2). In S-GC all meteorological fields are explicitly specified by MERRA-2, using the

405 same 72-layer vertical grid. The only exception is the specific humidity in the stratosphere, which is computed online. In C-

406 CC and C-GC, we use the "specified dynamics" (SD) configuration of CAM6 in which 3-D temperature, 3-D wind velocities,

407 surface pressure, surface temperature, surface sensible heat flux, surface latent heat flux, surface water flux, and surface

408 stresses are provided by MERRA-2 on a truncated 56-layer vertical grid. These variables are nudged with a relaxation time of

409 50 hours, resulting in a relatively "loose" nudging strength. All other fields (e.g. cloud fraction) are computed using the CAM

410 physics routines. This includes convection. Whereas S-GC computes convective transport from archived convective mass

411 fluxes and calculates scavenging within the updraft (Wu et al., 2007), convective transport in both C-CC and C-GC is

412 calculated in CAM6 using the CLUBB-SGS scheme for shallow convection and the Zhang-McFarlane scheme for deep

413 convection. Scavenging within the convective updraft is not simulated explicitly.

414

415 Water vapor in C-GC is initialized from the specific humidity "Q" restart variable, which is identical to the one used for C-

416 CC; after this point humidity is calculated based on the moist processes represented explicitly in CAM's physics package. The

417 GEOS-Chem CTM does not calculate water vapor in the troposphere, instead prescribing specific humidity directly from

418 MERRA-2 output. Mixing ratios of water vapor in C-CC and C-GC are therefore identical to that in S-GC at initialization

419 time, but from that point onwards may diverge.

420

421 Emissions are harmonized between the three models, with all three configurations using HEMCO to calculate emissions fluxes.

422 Surface anthropogenic emissions are provided from CEDS and are identical between all three models, apart from small

423 differences in effective emissions from ships due to parameterized plume processing (Vinken et al., 2011). Simulated

424 anthropogenic surface emissions of nitrogen oxides are 145-148 Tg(NO$_2$) in each of the three models. Aviation emissions are

14

425 calculated in all three models based on the AEIC 2005 emission inventory, contributing a further 2.7 Tg NO_2 in addition to

426 other species (Simone et al., 2013).

427

428 Lightning emissions are calculated in C-CC and C-GC using the online parameterization described in Section 2.3.3, while

429 lightning emissions in S-GC are calculated using archived flash densities and cloud top heights (Murray et al., 2012). Total

430 emissions are 13 Tg NO in all three models, with less than 2% difference in total. Biogenic emissions are calculated in C-CC

431 and C-GC using the embedded MEGAN emissions module in CESM, which differs slightly from the implementation in S-GC

432 and will produce different emissions due to different vegetation distributions. Total biogenic emissions in S-GC and C-GC are

433 shown in Table 2. In all three simulations we use the "AeroCom" volcano emissions implemented in HEMCO.

434

435 *Table 2. Annual global biogenic emission totals in standalone GEOS-Chem (S-GC) compared to in GEOS-Chem implemented in CESM (C-*
436 *GC).*

Species	Name in GEOS-Chem	S-GC (Tg/year)	C-GC (Tg/year)
Acetone	ACET	48.2	42.7
Acetic acid	ACTA	-	3.86
Acetaldehyde	ALD2	17.9	20.8
Lumped alkanes >= C_4	ALK4	-	0.16
Ethylene	C2H4	-	30.4
Ethane	C2H6	0.21	0.34
Propane	C3H8	-	0.03
Formaldehyde	CH2O	-	5.14
Carbon monoxide	CO	-	88.8
Ethanol	EOH	17.9	20.8
Limonene	LIMO	9.11	11.0
α/β-pinene, sabinene, carene	MTPA	81.5	98.6
Other monoterpenes	MTPO	38.6	40.8
Isoprene	ISOP	397.6	502
Methanol	MOH	-	119
Toluene	TOLU	-	1.57
Lumped alkenes >= C_3	PRPE	24.2	22.3

437

438 Mobilization of mineral dust is calculated in all three models using the DEAD scheme (Zender, 2003). In C-CC and C-GC,

439 the online implementation in CESM is employed, resulting in total natural mineral dust emissions of 5984 Tg/year. A brief

440 discussion of dust emissions in CESM is provided in the SI. In S-GC, natural mineral dust emissions are calculated online

441 using the same scheme but with a different scaling and at a slightly different grid resolution, resulting in total emissions of

442 1390 Tg/year.

443

444 Emissions of sea salt are calculated online in CESM for C-GC and C-CC, while S-GC uses a pre-calculated (offline) inventory

445 of sea-salt emissions, as well as sea-salt bromine and chloride. Emissions of sea-salt bromine in C-GC are calculated based on

446 the offline inventory rather than the calculated emissions of sea salt, and therefore do not scale correctly with the estimated

447 sea-salt emissions from CESM (see Table 3). This will be resolved as part of future work.

448

449 *Table 3. Annual global emissions of sea salt aerosols (fine and coarse) and bromine in sea salt for C-GC and S-GC. The names of the tracers*
450 *used to represent these species in GEOS-Chem are provided in brackets.*

Species	C-GC (Tg/year)	S-GC (Tg/year)
Fine sea-salt (SALA)	93.0	59.1
Coarse sea-salt (SALC)	2780	3576
Bromine in fine sea-salt (BrSALA)	0.166	0.126
Bromine in coarse sea-salt (BrSALC)	10.1	7.54

451

452 Finally, for long-lived species such as CFCs we use the shared socio-economic pathway 2-4.5 (SSP2-4.5) set of surface

453 boundary conditions in both C-GC and C-CC. In comparisons against S-GC we use historical emissions from the World

454 Meteorological Organization's 2018 assessment of ozone depletion (Fahey et al., 2018). However, this difference is unlikely

455 to significantly affect simulation output given the short duration of the simulations.

456 **3.2   Model intercomparison**

457 We first compare the global distribution of ozone and aerosols between C-GC, S-GC, and C-CC. Section 3.2.1 evaluates the

458 vertical and latitudinal distribution of ozone and two related species (water vapor and the hydroxyl radical), followed by the

459 global distribution of ozone at the surface in each model configuration (Section 3.2.2). A similar evaluation of differences in

460 zonal mean and surface aerosol concentrations follows (Section 3.2.3).

461

462 To understand the causes of these differences, we compare the global distribution of reactive nitrogen and halogen species in

463 each model configuration (Section 3.2.4). When comparing halogen distributions we consider only bromine and chlorine

464 distributions, as iodine is not simulated in this version of CAM-chem. Differences in the total atmospheric burden and vertical

465 distribution of these families provides information regarding differences in removal processes. Differences in their internal

466 partitioning (e.g. between NO_x and HNO_3) provide information regarding the representation of atmospheric chemistry.

3.2.1 Ozone

Figure 2 shows the annual mean mixing ratio of stratospheric ozone simulated by each of the three model configurations. At 10 hPa in the tropics, where ozone mixing ratios reach their peak, the three configurations agree to within 10% suggesting a reasonable representation of stratospheric ozone. However, near the tropopause the three configurations diverge. C-GC simulates mixing ratios of ozone around the tropopause which are 20% lower than C-CC at all latitudes. This difference may be the result of greater mixing ratios of reactive bromine in the C-GC troposphere than in C-CC (see Section 3.2.4.2).
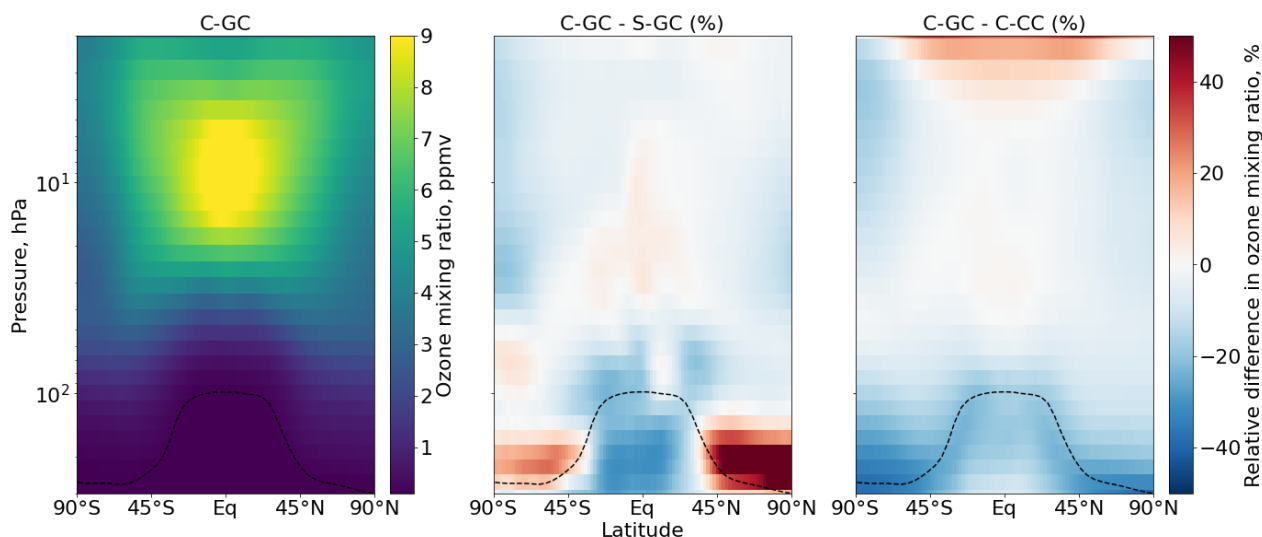
Figure 2. Comparison of stratospheric ozone simulated with CESM running GEOS-Chem (C-GC) to standalone GEOS-Chem (S-GC) and CESM running CAM-chem (C-CC). Left column: absolute values estimated with C-GC. Center column: relative difference between C-GC and S-GC. Right column: relative difference between C-GC and C-CC. Red (blue) shading means that C-GC estimated a higher (lower) value than the other model.

Comparison of C-GC to S-GC shows a different pattern, with mixing ratios 20% lower than S-GC near the tropical tropopause but more than 50% greater in the extratropical lower stratosphere. The absence of this pattern from the comparison against C-CC implies that the cause is likely to be related to factors which are common between C-GC and C-CC, such as the representation of meteorology.

To quantify and understand these differences in stratospheric ozone, we analyze concentrations of three different related compounds from the surface to the stratosphere: ozone itself, the hydroxyl (OH) radical, and water vapor. Since OH is produced from water vapor and (indirectly) ozone, these three compounds can collectively be used to understand some of the differences between C-GC, S-GC, and C-CC. Later analyses will focus on NO_x, bromine, and chlorine, each of which also strongly affect tropospheric and stratospheric concentrations of ozone.

489   The upper row of Figure 3 shows the distribution of ozone as represented by C-GC (left), and the difference when compared

490   to S-GC (center) or C-CC (right). Comparing first to C-CC, C-GC estimates mixing ratios of ozone which are 30% lower at

491   the surface (averaged over all latitudes) and throughout the extratropical troposphere. This is consistent with previous work

492   which showed that ozone simulated by GEOS-Chem to match the KORUS-AQ campaign had a normalized mean bias of -

493   26%, compared to -9% in CAM-chem. The lower concentrations of ozone are evident in both hemispheres, although

494   differences fall to zero in the tropical free troposphere. Ozone mixing ratios around the tropopause are also lower in C-GC

495   than in C-CC by 15-20%.

496

497   Comparing to the differences between C-GC and S-GC provides some insight into possible causes for these discrepancies.

498   Near-surface ozone in C-GC in the southern hemisphere is also 30-40% lower than in S-GC, suggesting a potential common

499   cause for the differences with C-CC. However, in the northern extratropical troposphere below 400 hPa, zonal mean differences

500   between C-GC and S-GC are consistently less than 10%. Ozone concentrations are also lower in the tropical mid-troposphere

501   in C-GC than in S-GC by 15-25%, whereas concentrations were well matched in this region between C-GC and C-CC. In the

502   lower stratosphere, ozone concentrations in C-GC are instead greater than in S-GC, with the difference in the northern

503   extratropical lower stratosphere exceeding 50%. The global ozone burden in C-GC is within 1.5% of that estimated by S-GC,

504   while C-CC has a total atmospheric ozone burden 15% greater than C-GC.

505

506   Differences in tropospheric NO_y and halogens, in particular the higher loading of BrO in C-GC, may explain some of these

507   differences (see Section 3.2.4). However, another possible factor in these differences in ozone is differences in water vapor

508   distribution. The bottom row of Figure 3 shows the annual average simulated distribution of water vapor in C-GC, and the

509   difference relative to S-GC and C-CC. Water vapor concentrations are approximately equal between C-GC and C-CC, since

510   the representation of moist physics in the two models is identical. However, differences of up to 20% arise around the

511   tropopause, possibly due to the different representation of stratospheric water chemistry and settling of stratospheric aerosol

512   (including ice).

513

514   The differences between C-GC and S-GC are larger. Outside of the tropics and below the tropopause, water vapor

515   concentrations are up to 30% greater in C-GC than in S-GC. Differences are smaller in the tropics, but in the tropical upper

516   troposphere water vapor concentrations are instead 15% lower in C-GC than in S-GC. This may be part of the reason that

517   water vapor concentrations in the extratropical lower stratosphere are more than 50% lower in C-GC than in S-GC, since the

518   tropical upper troposphere is the source of water vapor to the stratosphere. This is the same region in which C-GC calculates

519   ozone mixing ratios which are more than 50% greater than in S-GC, potentially due to the lower concentration of water vapor

520   (an indirect sink for ozone).

521

522 These differences arise due to the different representation of moist processes between CAM's physics package (used in both
523 C-GC and C-CC), and GEOS, which produces MERRA-2 and therefore is represented in S-GC. For example, although total
524 annual average precipitation agrees to within 10% between the models, the mean volumetric cloud fraction in C-GC and C-
525 CC is 15%, compared to 8% in S-GC. Meanwhile the area-averaged cloud water content and cloud ice content are 57% and
526 38% greater in S-GC than in C-GC (or C-CC).
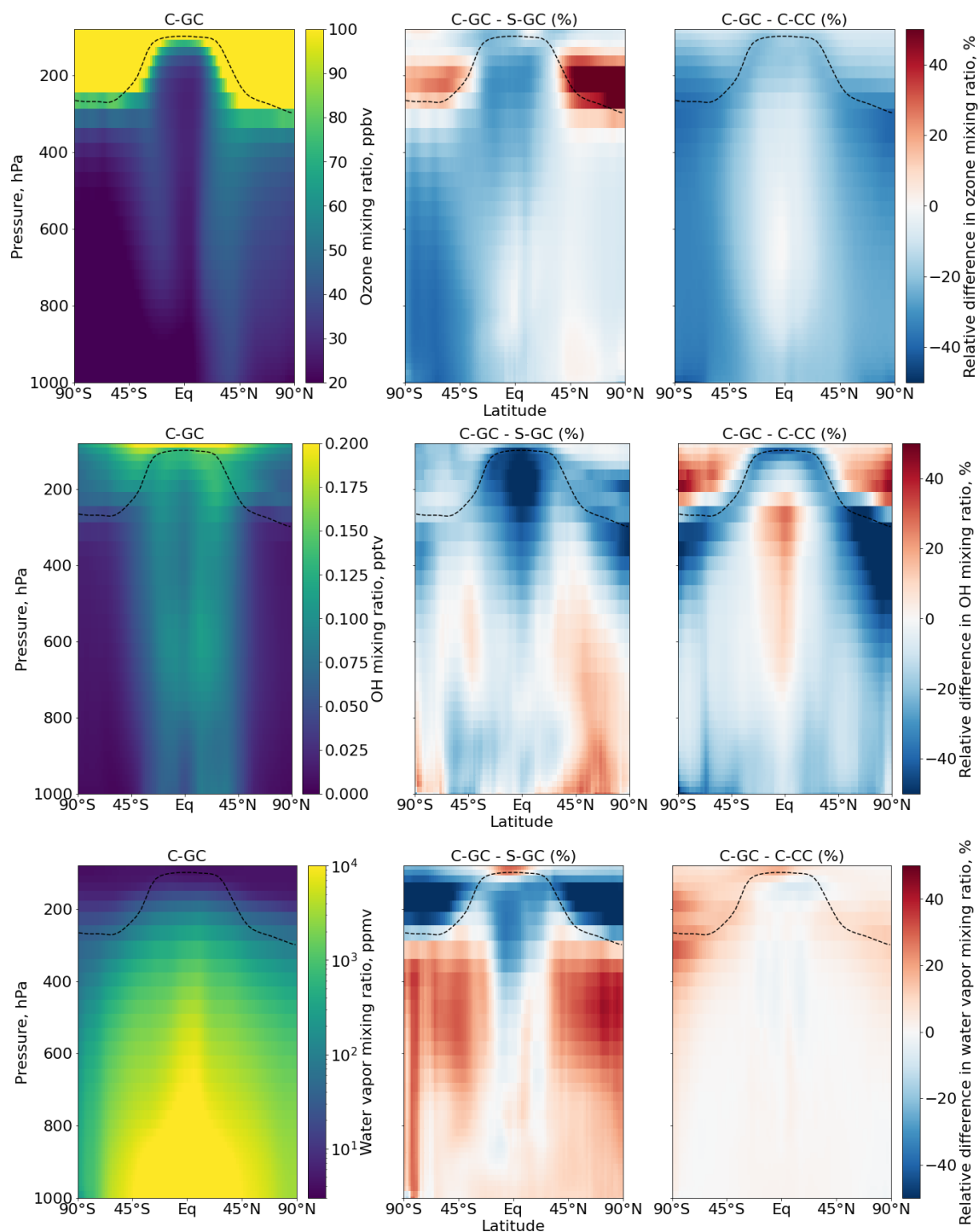
527 *Figure 3. Comparison of atmospheric composition simulated with CESM running GEOS-Chem (C-GC) to standalone GEOS-Chem (S-GC)*
528 *and CESM running CAM-chem (C-CC). Different rows show different constituents, while different columns show different model results.*
529 *Top row: ozone. Middle row: OH radical. Bottom row: water vapor. Left column: absolute values estimated with C-GC. Center column:*

530 *relative difference between C-GC and S-GC. Right column: relative difference between C-GC and C-CC. Red (blue) shading means that C-*
531 *GC estimated a higher (lower) value than the other model.*

532 Differences in ozone and water vapor result in differences in concentrations of OH, as shown in the middle row of Figure 3.
533 The global OH atmospheric burden is ~10% lower in C-GC than in S-GC, but this difference is not evenly distributed.
534 Differences in OH concentrations can be roughly considered to be the product of differences in ozone and differences in water
535 vapor, since both are needed to create OH (along with UV radiation). In the tropical troposphere, OH concentrations are more
536 than 50% lower in C-GC than in S-GC, likely due to a relative lack of both ozone and water vapor. However in the northern
537 mid- and upper latitudes below 900 hPa, OH concentrations are 10-20% greater in C-GC than in S-GC. This reflects the greater
538 water vapor concentrations and roughly equal ozone concentrations between the two models.

539 **3.2.2 Surface ozone**

540 Figure 4 compares the simulated, annually-averaged surface ozone mixing ratios as estimated by C-GC, S-GC, and C-CC. We
541 find that, when globally averaged, C-GC predicts a lower surface ozone mixing ratio than either C-CC or S-GC. The difference
542 compared to S-GC peaks over Southern Africa and over Northern India, reaching an absolute difference of 12 ppbv. Averaged
543 over each hemisphere, C-GC estimates a lower surface ozone mixing ratio than S-GC by 4.9 ppbv and 2.2 ppbv in the Southern
544 Hemisphere and Northern Hemisphere respectively. This varies between the land and oceans. In the Northern Hemisphere, we
545 observe no difference in surface ozone mixing ratio over the oceans, while a decrease of ~3 ppbv can be found over North
546 America, Europe and East Asia.

547
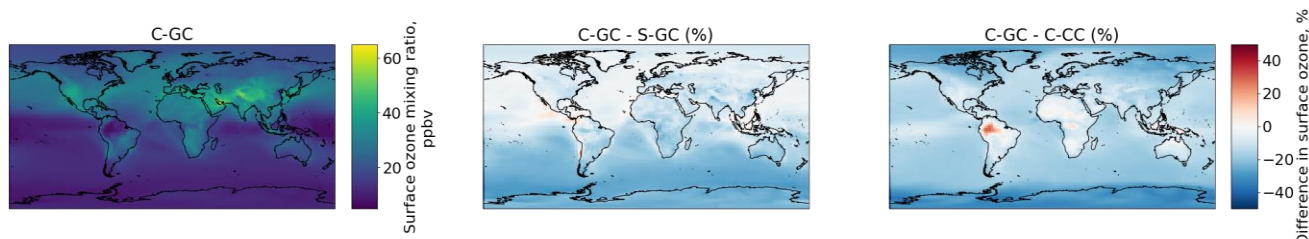
548
549 *Figure 4. Comparison of the annually averaged surface ozone mixing ratios simulated with CESM running GEOS-Chem (C-GC) to*
550 *standalone GEOS-Chem (S-GC) and CESM running CAM-chem (C-CC). Red (blue) shading means that C-GC estimated a higher (lower)*
551 *value than the other model.*

552 The difference between C-GC and C-CC does not show the same hemispheric asymmetry, and a larger difference over oceans
553 than over land. We find that C-GC estimates 5.4 and 7.9 ppbv less ozone than C-CC in the Southern and Northern Hemispheres
554 respectively. The pattern indicated in Figure 4 suggests that bromine from sea salt may be the principal cause of the differences
555 in surface ozone between C-GC and C-CC, whereas differences between C-GC and S-GC are likely to be related to
556 anthropogenic emissions given the hemispheric asymmetry. The 20-30% increase in ozone over the Amazon in C-GC related
557 to C-CC may instead be related to differences in biogenic emissions.

558

21

559   In addition to annual averages, we also consider seasonal variations of surface ozone. Figure 5 presents parity plots of monthly-

560   averaged surface ozone mixing ratios for January and July comparing C-GC to S-GC and C-CC, after outputs from all three

561   model configurations were remapped to a common 2°×2.5° grid. In January, we find a correlation coefficient of 0.87 and slope

562   of 0.93 between C-GC and S-GC. In July this agreement is worsened, with a correlation coefficient of 0.76 and a slope of 0.91.

563   This indicates that the sources of differences in surface ozone mixing ratios between C-GC and S-GC are magnified during

564   boreal summer. There is also a distinctive "hot spot" in the July parity plot, with a large cluster of grid cells showing mixing

565   ratios in the range 20-25 ppbv in S-GC but 15-20 ppbv in C-GC. Further research is needed to establish the origin of this

566   cluster, which does not occur during boreal winter.

567

568

569
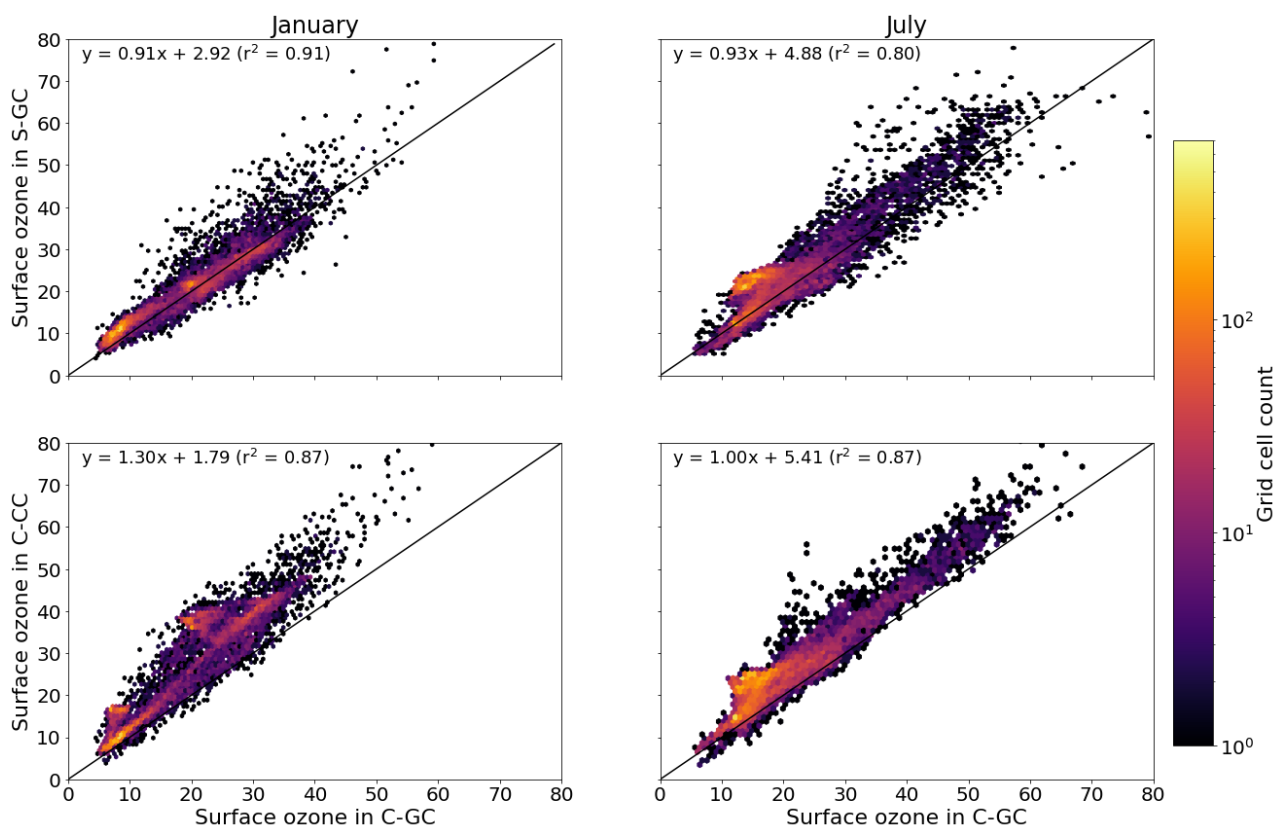
Figure 5. Parity plots of surface ozone mixing ratios, expressed in ppbv, for January (left) and July (right) comparing C-GC on the X axis
to S-GC (top) and C-CC (bottom) on the Y axis. Fitting parameters are shown in the top left corner for both months. All panels share the
same color scale.

573   Comparison between C-GC and C-CC shows a different pattern. The line of best fit between C-CC and C-GC indicates 30%

574   greater ozone in C-CC in January than in C-GC (y ~ 1.3x), but no such normalized mean bias is present in July (y ~ 1.0x). As

575   with the comparison of C-GC to S-GC, the absolute bias is greater in July than in January, but the correlation between C-CC

576 and C-GC does not worsen between the two months ($r^2 = 0.87$). This may indicate the strength of the effect of meteorology

577 and non-chemistry processes in the seasonality of simulated surface ozone.

3.2.3 Aerosols

579 Figure 6 shows the zonal mean mass concentration of sulfate aerosol as simulated in each of the three model configurations.

580 In C-GC and C-CC, this is calculated as the sum across all aerosol size bins, whereas S-GC uses a bulk representation.

581
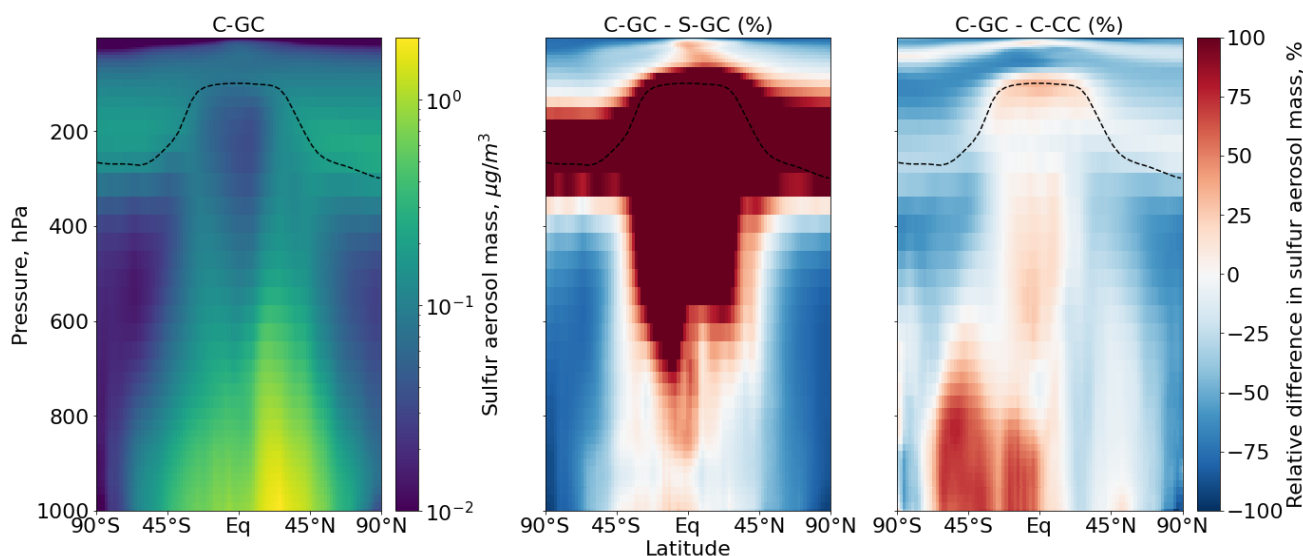
Figure 6. Comparison of sulfate aerosol mass concentration as simulated with CESM running GEOS-Chem (C-GC) to standalone GEOS-Chem (S-GC) and CESM running CAM-chem (C-CC). Left: absolute values estimated with C-GC. Center: relative difference between C-GC and S-GC. Right: relative difference between C-GC and C-CC. Red (blue) shading means that C-GC estimated a higher (lower) value than the other model. Differences are restricted to ±100% for clarity.

586 Between 45°S and 45°N, and below 800 hPa, C-GC more closely follows S-GC with regards to sulfate aerosol mass. Compared

587 to C-CC, sulfate aerosol mass is ~50% greater in Southern latitudes with differences being greatest over the emission. This is

588 despite emissions of DMS from the ocean being calculated the same way in all three model configurations. However, elsewhere

589 the concentration of sulfate in C-GC more closely follows that in C-CC, likely due to the common representation of sulfate

590 aerosol in MAM4 and differences in the representation of convective scavenging between CESM and standalone GEOS-Chem.

591 Concentrations of sulfate in the tropical upper troposphere and extratropical lower stratosphere in C-GC exceed those in S-GC

592 by over 100%, whereas comparison to C-CC show differences of ±25%.

593

23
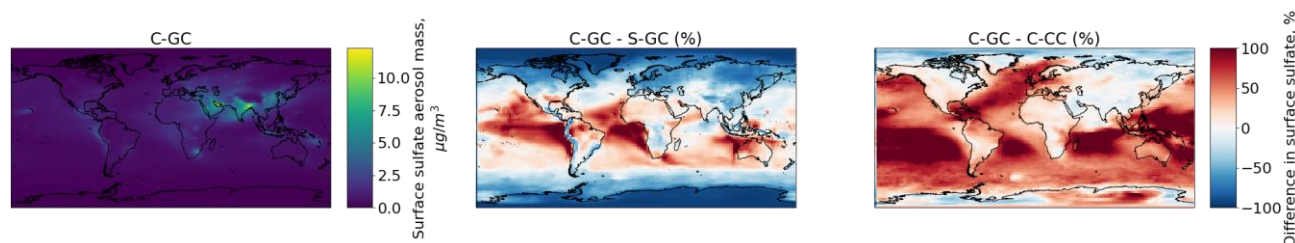
Figure 7. Comparison of the annually averaged surface mass concentration of sulfate aerosol simulated with CESM running GEOS-Chem (C-GC) to standalone GEOS-Chem (S-GC) and CESM running CAM-chem (C-CC). Red (blue) shading means that C-GC estimated a higher (lower) value than the other model.

This is further illustrated in Figure 7, which shows the surface concentration of sulfate aerosol in each model configuration. C-GC simulated greater concentrations in the intertropical convergence zone than in S-GC, but in these regions agrees more closely with C-CC. Elsewhere in the tropics the agreement between C-GC and S-GC is stronger, whereas surface concentrations of sulfate aerosol over (e.g.) the Southern Pacific exceed those in C-CC by over 100%. At high latitudes and over land the agreement between C-GC and C-CC is again stronger than in S-GC, although this varies by location.
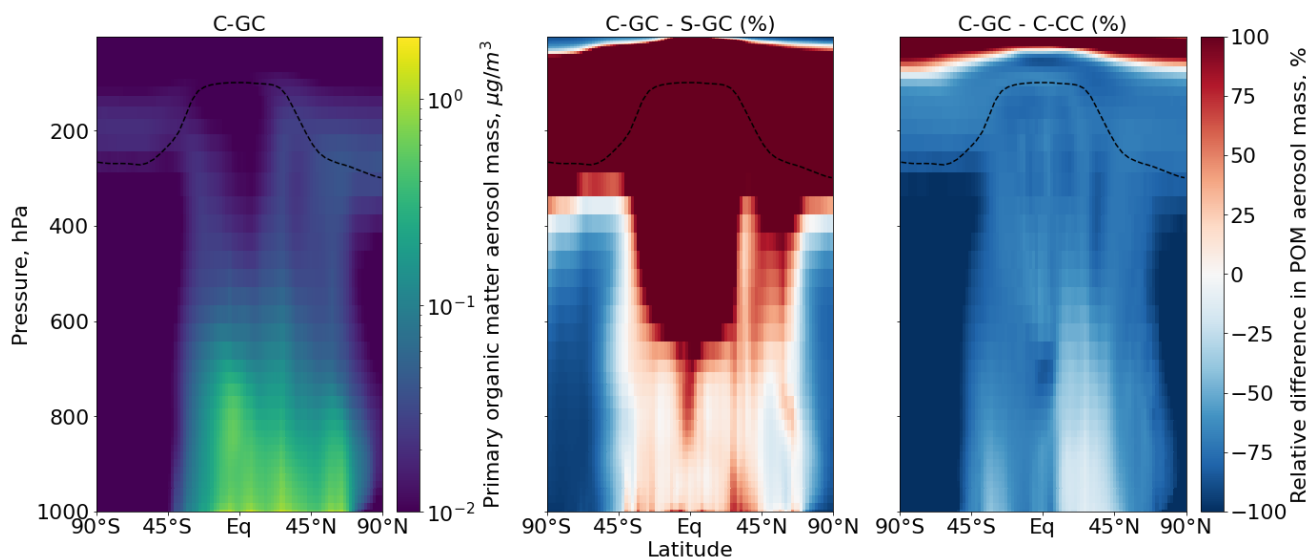
Figure 8. Comparison of primary organic matter aerosol mass concentration as simulated with CESM running GEOS-Chem (C-GC) to standalone GEOS-Chem (S-GC) and CESM running CAM-chem (C-CC). Left: absolute values estimated with C-GC. Center: relative difference between C-GC and S-GC. Right: relative difference between C-GC and C-CC. Red (blue) shading means that C-GC estimated a higher (lower) value than the other model.

We also show the zonal mean concentrations of primary organic matter (POM) aerosol in each configuration (Figure 8). POM in C-GC and C-CC is calculated as the sum of the POM aerosol size bins, whereas in S-GC it is the sum of the hydrophobic and hydrophilic organic carbon species. As with sulfate aerosol, C-GC and S-GC agree to within 25-50% in the tropics below 800 hPa, but C-GC simulates concentrations of POM which are over 100% greater than S-GC in the tropical upper troposphere and extratropical lower stratosphere. This is again likely due to differences in the representation of convective scavenging. C-

24

613 GC also simulates concentrations of POM which are lower than C-CC throughout the entire troposphere. This is likely due to

614 differences in the implementation of POM emissions between C-CC and C-GC, where emissions of POM in C-CC are 29%

615 lower and occur as accumulation-mode rather than primary organic mode aerosol.

616 **3.2.4   Reactive nitrogen (NO$_y$), bromine (Br$_y$), and chlorine (Cl$_y$)**

617 To better understand the source of differences in ozone and aerosols described above, we now investigate differences in

618 reactive nitrogen (NO$_y$) and halogen families (Br$_y$ and Cl$_y$).

619

620 **3.2.4.1   Reactive nitrogen (NO$_y$)**

621 We compare the total concentration and partitioning of reactive nitrogen species in each model configuration, including

622 nitrogen oxides (NO$_x$) and its reservoir species (collectively NO$_y$). We first compare results in the stratosphere, followed by

623 an evaluation of concentrations and partitioning below 100 hPa. Concentrations of nitrate aerosol concentrations are estimated

624 in CAM-chem using a simplified approximation (Lamarque et al., 2012), and particulate nitrate is typically not considered to

625 be simulated by CAM-chem (e.g. Park et al (2021)). We therefore do not include it in this analysis.

626
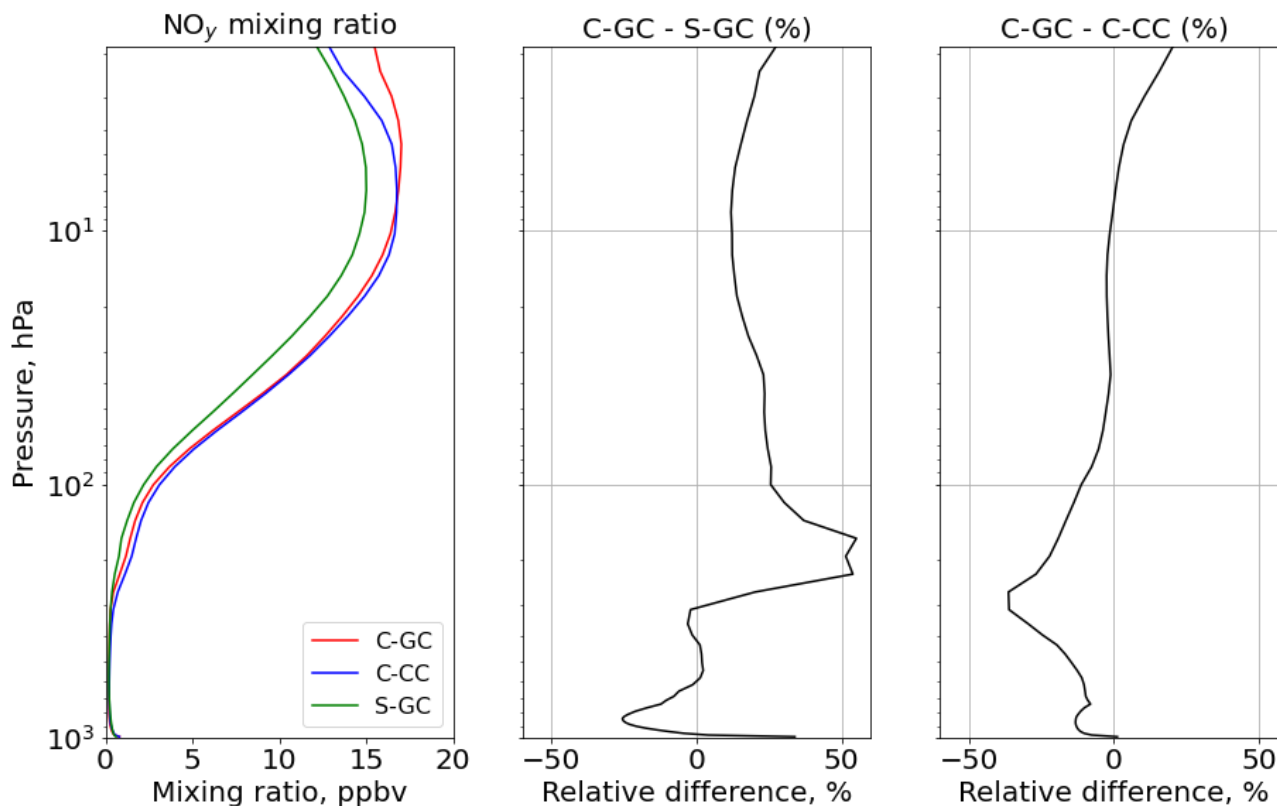
627

628 *Figure 9. Global annual mean mixing ratio of total reactive nitrogen (NO_y) as a function of altitude. Left: Vertical profile of NO_y mixing*
629 *ratio for C-GC (red), C-CC (blue), and S-GC (green). Middle: Relative difference in NO_y mixing ratio between C-GC and S-GC. Right:*
630 *Relative difference in NO_y mixing ratio between C-GC and C-CC.*

631 Figure 9 shows global mean NO_y at each altitude for C-GC, C-CC, and S-GC. Comparing C-GC to C-CC first, differences in

632 total NO_y are less than ±30% at all altitudes. Between 100 and 10 hPa, C-GC differs from C-CC by less than 10%. Above 10

633 hPa, the vertical profile more closely matches S-GC than C-CC. The difference between C-GC and C-CC increase from -2%

634 at 10 hPa to +20% at the top of the model, compared to an increase from 10% to 25% when comparing C-GC to S-GC. At

635 lower altitudes C-GC more closely follows C-CC than S-GC, with differences between C-GC and S-GC exceeding 50%

636 between 200 and 300 hPa. The global NO_y burden in C-GC (2.74 TgN) is closer to that in S-GC (2.84 TgN) than C-CC (3.01

637 Tg), likely due to the stronger influence of the troposphere on this quantity.

638

639 Figure 10 shows the speciation of NO_y as a function of altitude in each model from the surface to 0.1 hPa. At altitudes above

640 100 hPa, the dominant contributors to NO_y in all three model configurations are NO, NO_2, HNO_3, and N_2O_5, although $ClNO_3$

641 contributes significantly between approximately 80 and 5 hPa. Between 10 and 200 hPa ratios of NO to NO_2 are approximately

642 consistent between the models, lying in the range 0.35 to 0.50. This suggests broad consistency in actinic flux and ozone

643 concentrations, given their role in controlling $NO:NO_2$ ratios in the stratosphere (Cohen and Murphy, 2003).

644

645 By contrast, partitioning between NO_x and HNO_3 differs significantly between the three models. At 10 hPa, HNO_3 constitutes

646 20% of total NO_y in C-GC but 23% in both C-CC and S-GC. This fraction increases with decreasing altitude at differing rates.

647 At 200 hPa, HNO_3 constitutes 60 and 63% of NO_y in C-GC and S-GC respectively, but 78% of NO_y in C-CC. One possible

648 cause of these discrepancies is heterogeneous chemistry. GEOS-Chem (in both S-GC and C-GC) uses a different representation

649 of N_2O_5 hydrolysis than CAM-chem, but the CESM-driven simulation include a more detailed representation of the sulfate

650 aerosol size distribution through MAM4.

651
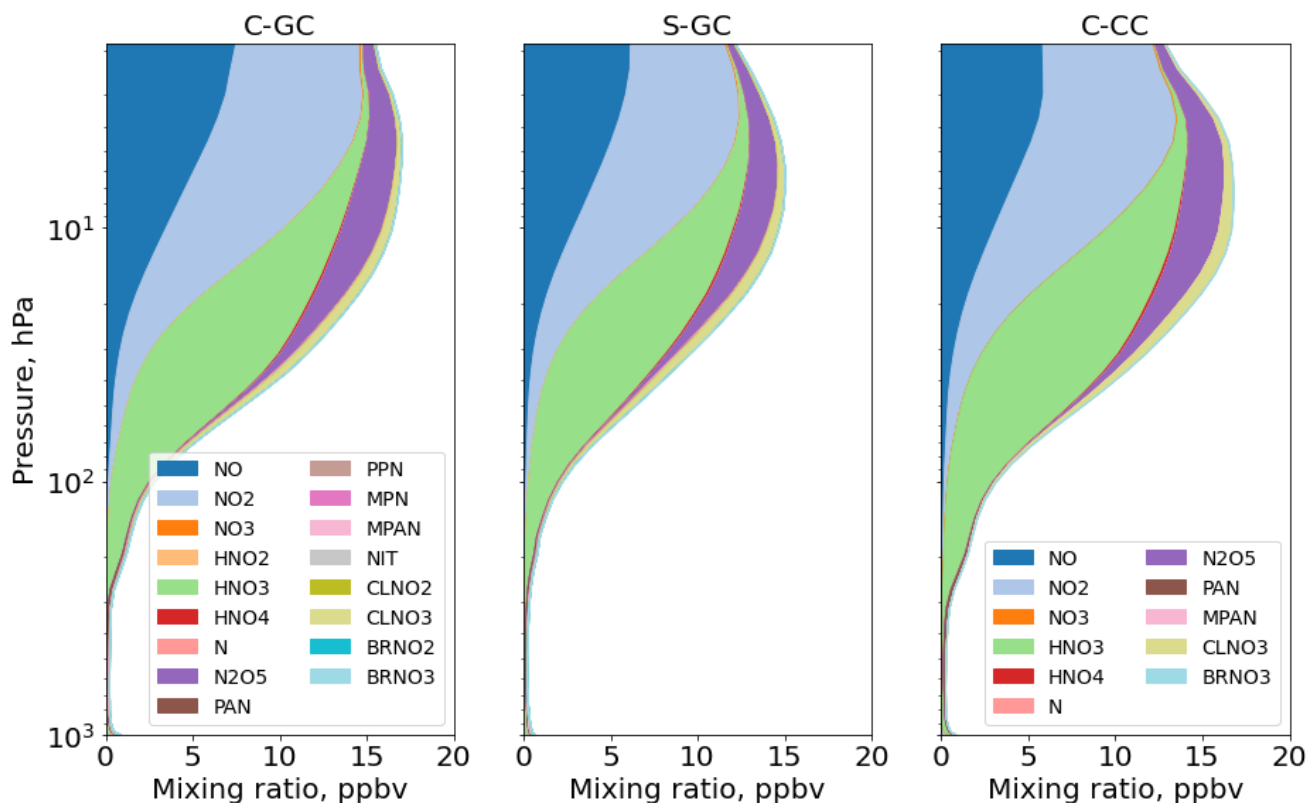
Figure 10. Global annual mean speciation of NO_y as a function of altitude. Results are shown from C-GC (left), S-GC (middle), and C-CC (right) from the surface up to the model top (~2 hPa). Values correspond to the number of N atoms present, such that (e.g.) the mixing ratio of N_2O_5 is multiplied by 2.

Figure 11 provides a closer look at the speciation of NO_y at altitudes below 100 hPa. NO_y above 200 hPa is predominantly NO_x, HNO_3, and N_2O_5, at altitudes. However, between 200 and 900 hPa the dominant contributors are HNO_3 and peroxyacetyl nitrate (PAN), although the C-GC and S-GC simulations also show a significant contribution from nitrate aerosol (NIT) and $BrNO_3$. Below 900 hPa, NO and NO_2 once again become significant contributors to total NO_y. At these lower altitudes C-GC more closely follows C-CC than S-GC, with differences in total NO_y between C-GC and S-GC exceeding 50% between 200 and 300 hPa. Since surface emissions of NO_x are nearly identical between the three configurations and lightning NO_x emissions are identical between C-GC and C-CC, differences below 100 hPa are most likely related to the representation of wet deposition and of nitrate aerosol.

667

668
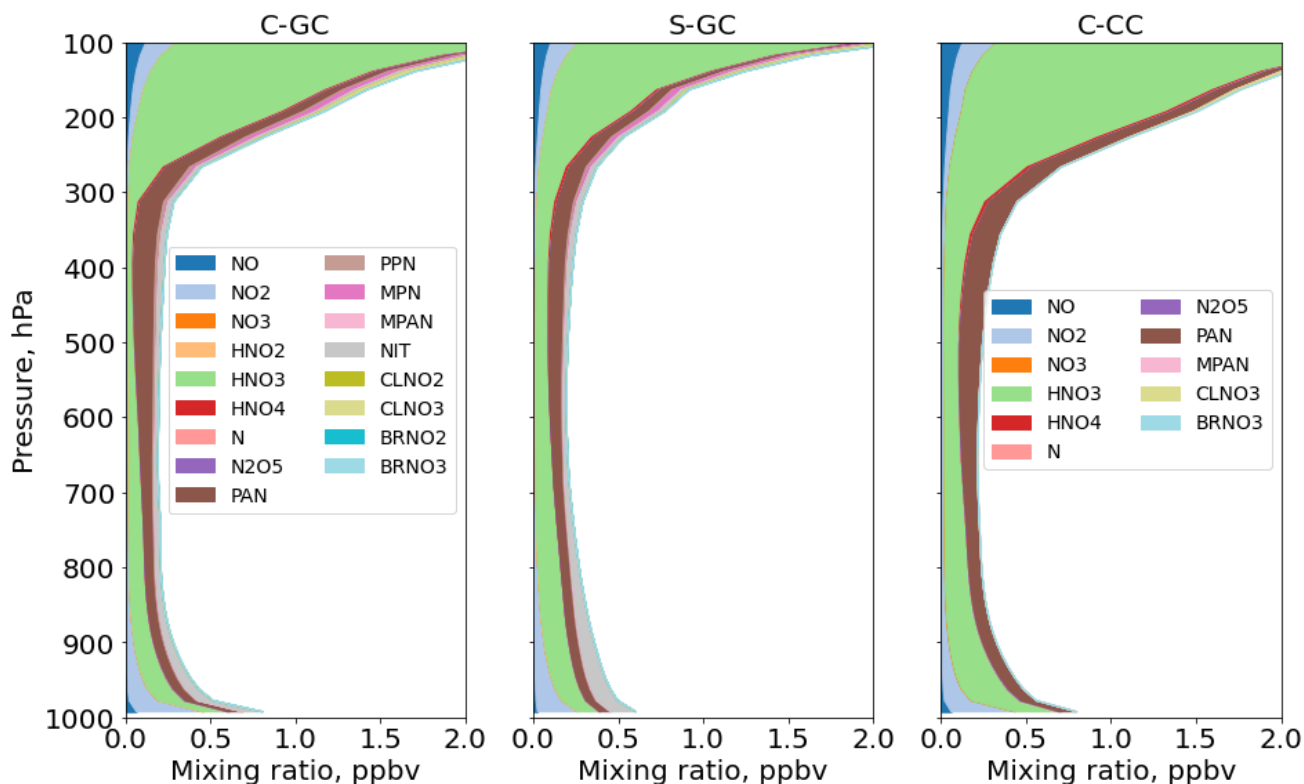
Figure 11. As in Figure 10, but showing only the 10^3-10^2 hPa pressure range.

670 Although the total NO$_y$ mixing ratio in C-GC generally more closely follows C-CC than S-GC as discussed, the speciation in
671 C-GC more closely follows that in S-GC at lower altitudes. At 200 hPa, the combination of NO$_x$, HNO$_3$, and PAN make up
672 86% of total NO$_y$ in C-GC and 84% in S-GC, but 96% in C-CC. At 500 hPa the contributions are 78%, 85%, and 97%
673 respectively. However, concentrations of PAN in C-GC more closely follow C-CC than S-GC. At 500 hPa, total PAN in C-
674 GC is 3% lower than the value in C-CC, but exceeds the value in S-GC by 38%. This may be due to the greater emissions of
675 biogenic VOCs in CESM than in the standalone GEOS-Chem (see Table 2), resulting in more NO$_x$ being bound into PAN for
676 long-range transport. We also find that HNO$_3$ concentrations in the mid-troposphere are lower in C-GC than in either C-CC or
677 S-GC. At 500 hPa, HNO$_3$ mixing ratios in C-GC are 43% lower than in S-GC and 52% lower than in C-CC. This does not
678 account for the conversion of HNO$_3$ in C-GC and S-GC to nitrate aerosol (NIT), which is not represented in C-CC.

679

680 Differences in mid-tropospheric HNO$_3$ between the models are most likely due to differences in the representation of wet
681 scavenging. In C-CC and C-GC, scavenging of gaseous species is handled by the Neu scheme, while scavenging of modal
682 aerosols is performed by MAM (Neu and Prather, 2012). Any aerosol species not handled by MAM, such as nitrate in C-GC,
683 are also scavenged using the Neu scheme. In C-GC and C-CC, the Neu scheme calculations are performed at the same time as

684   the chemistry and after convective transport, while scavenging of MAM aerosols is performed before. Thus, all species that

685   undergo wet deposition in the Neu scheme are not removed during convective transport. This leads to soluble species and

686   aerosols being carried to higher altitudes without being convectively scavenged.

687
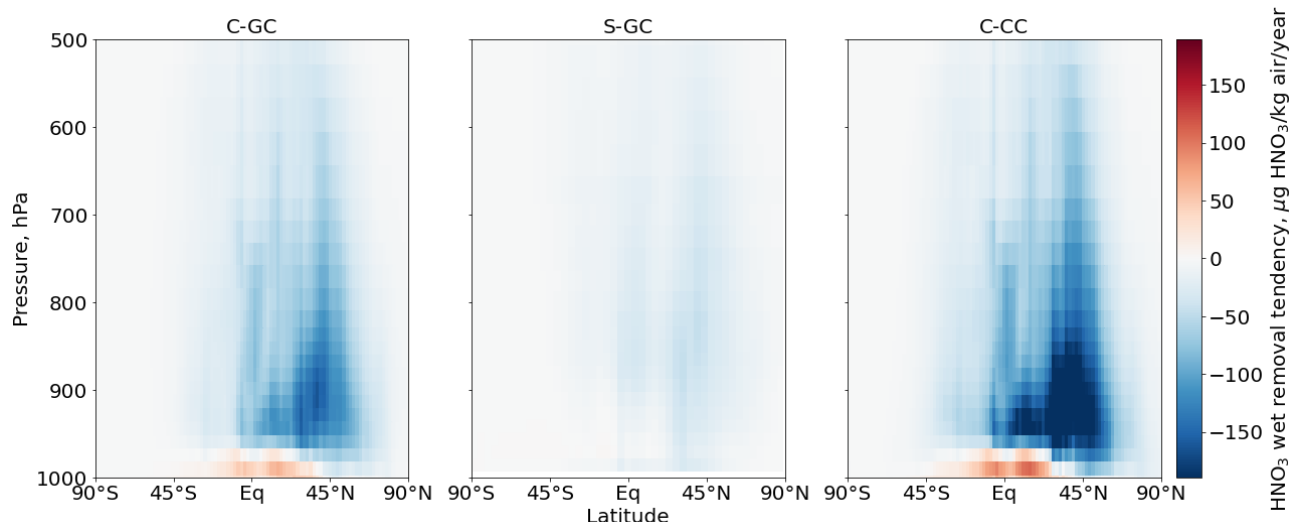
688
689   *Figure 12. Annual zonal mean of nitric acid wet removal tendencies for C-GC (left), S-GC (middle), and C-CC (right).*

690   Figure 12 shows the calculated wet removal rate of HNO$_3$ in all three models. Positive values correspond to rain re-evaporation

691   at low altitudes re-releasing dissolved HNO$_3$. The Neu scavenging scheme in C-GC and C-CC results in an HNO$_3$ wet removal

692   rate which is four times higher in C-GC than in S-GC. This likely explains the greater depletion of HNO$_3$ in the mid-troposphere

693   calculated by C-GC compared to S-GC, as shown in Figure 11. Wet scavenging in C-CC is faster yet, with HNO$_3$ wet removal

694   rates approximately six times greater than in S-GC, and 50% greater than in C-GC. This is in part because the mixing ratio (or

695   fraction of total NO$_y$) of HNO$_3$ in the mid- and upper-troposphere as modeled in C-CC is greater than in either C-GC or S-GC,

696   but also because C-GC and S-GC simulate nitrate aerosol explicitly.

697
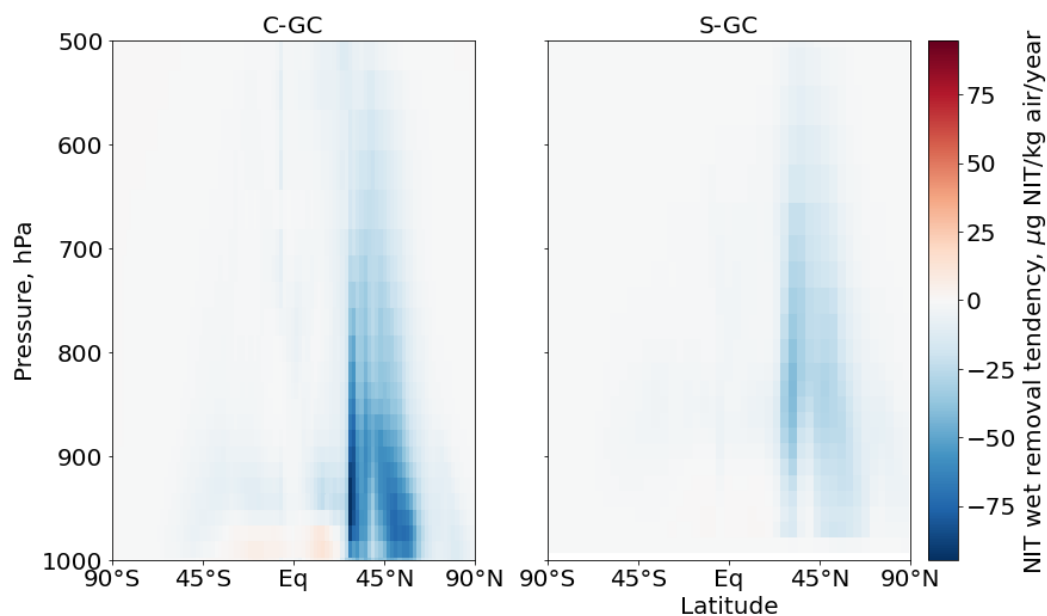
Figure 13. Annual zonal mean of nitrate aerosol (NIT) wet removal tendencies for C-GC (left) and S-GC (right). Nitrate aerosols are not modeled in CAM-chem.

The application of the Neu scheme to remove nitrate aerosol also affects removal of total NO_y in C-GC. Figure 13 shows the annual mean wet removal rates of the nitrate aerosol tracer NIT in C-GC and S-GC. The Neu scheme removes aerosol more rapidly than the scheme used in S-GC, and at lower altitudes.

Total HNO_3 removal in each model configuration are shown in Table 4. The total removal rate of NO_3^- is lowest in S-GC and highest in C-CC, consistent with the finding that total NO_y burdens are lower in S-GC than C-GC or C-CC. However, the removal rate of nitrate aerosol is lower in C-GC than in S-GC despite the greater wet removal rates shown in Figure 13 for C-GC. A possible explanation is that washout rates of nitrate aerosol are sufficiently high in both C-GC and S-GC that all nitrate aerosol is effectively removed, but that the faster washout of HNO_3 in C-GC results in less nitrate aerosol being available for removal.

Table 4. Total wet removal tendency of HNO_3 and nitrate aerosol in each model configuration. All values are given in units of Tg NO_3/yr.

	C-GC	S-GC	C-CC
HNO_3	82.0	71.3	119.6
Nitrate aerosol	20.4	22.7	-
Total NO_3^-	102.4	94.0	119.6

30

3.2.4.2   Reactive bromine (Br$_y$)

Figure 14 shows the annual average mixing ratio of total reactive bromine as a function of altitude in each of the three models. This does not include long-lived species such as halons or CH$_3$Br. A full listing is included in the legend of Figure 15.
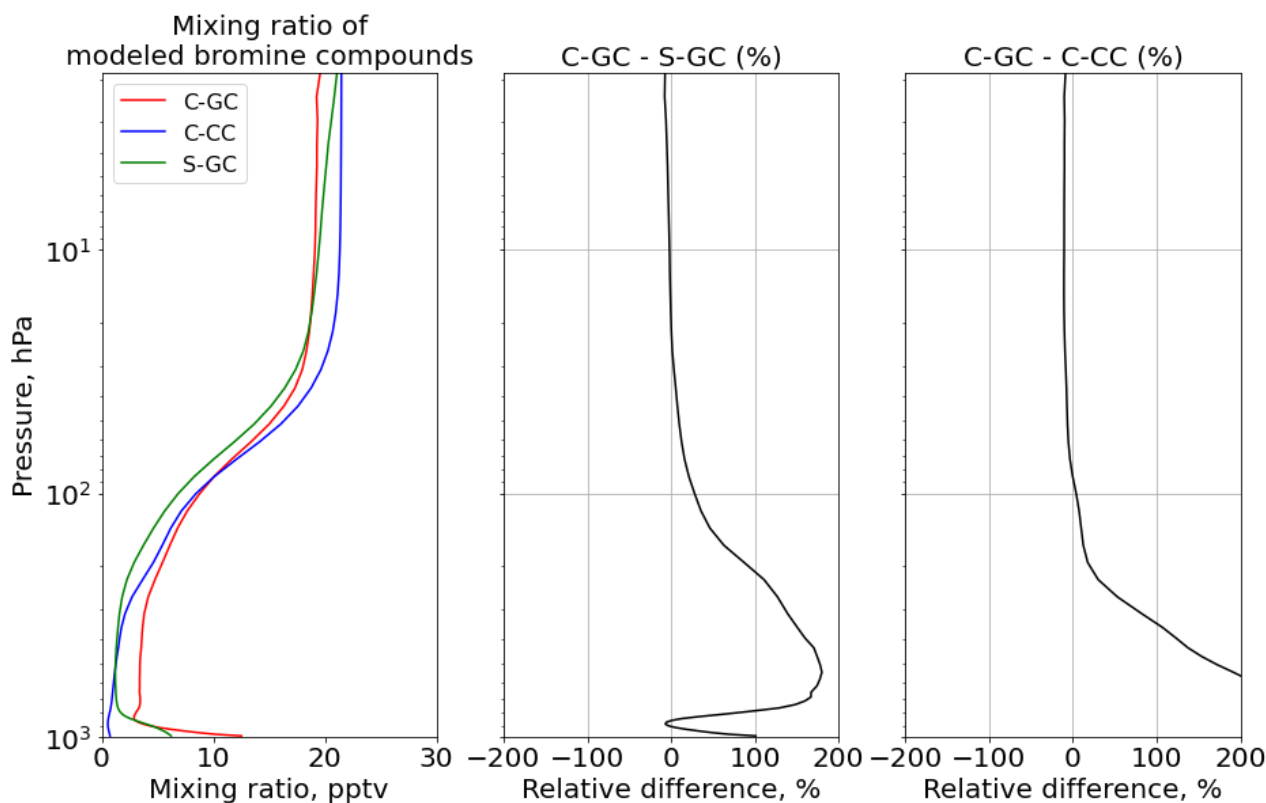
Figure 14. Global annual mean mixing ratio of reactive bromine as a function of altitude. Left: Vertical profile of total gaseous inorganic and organic bromine mixing ratio for C-GC (red), C-CC (blue), and S-GC (green). Middle: Relative difference in bromine-containing species mixing ratio between C-GC and S-GC. Right: Relative difference in bromine-containing species mixing ratio between C-GC and C-CC. Although relative differences between C-GC and C-CC exceed 1000% near the surface, the limits on the rightmost panel are clipped to allow comparison to the center panel.

Globally averaged, total Br$_y$ in C-GC is maximized at the surface, exceeding that from S-GC by 100%. This is partially explained by the greater emissions of sea salt bromine, although C-GC's annual emission of sea salt bromine is only 36% greater than that in S-GC (see Table 3). Since C-CC does not include short-lived bromine sources such as sea salt bromine, the difference between C-GC and C-CC exceeds 1000% at the surface.

In all three models the mixing ratio increases monotonically with altitude above 800 hPa due to the reaction of CH$_3$Br with OH. Br$_y$ falls sharply from 12 pptv at the surface in C-GC to 3 pptv at 900 hPa, but then increases again to 10 pptv at 100 hPa. This pattern is similar to that displayed by S-GC, although the decrease from the surface is less sharp and the absolute value lower in S-GC. Above 100 hPa the increase with altitude decreases, with values between 20 hPa and 2 hPa remaining roughly

734   constant in the range of 16-20 pptv. This is similar to the behavior shown by C-CC but differs from S-GC, in which Br_y

735   continues to rise with altitude – albeit more slowly. The net effect is that total Br_y in C-GC exceeds both C-CC and S-GC

736   below 100 hPa, but is lower than the value in either model above 10 hPa.

737

738   In addition to differences in total Br_y, the partitioning of Br_y also varies between the three models (Figure 15). The additional

739   near-surface bromine present in C-GC and S-GC is due to the presence of Br_2 and sea salt bromine (BrSALA and BrSALC,

740   representing bromine in fine and coarse-mode sea salt respectively). This provides a source of active bromine in the planetary

741   boundary layer which is not represented in C-CC, but in forms which are rapidly washed out. The greater concentrations of

742   Br_y near the surface as calculated by C-GC compared to S-GC are likely due to the greater emissions of sea salt bromine, as

743   shown in Table 3.

744

745
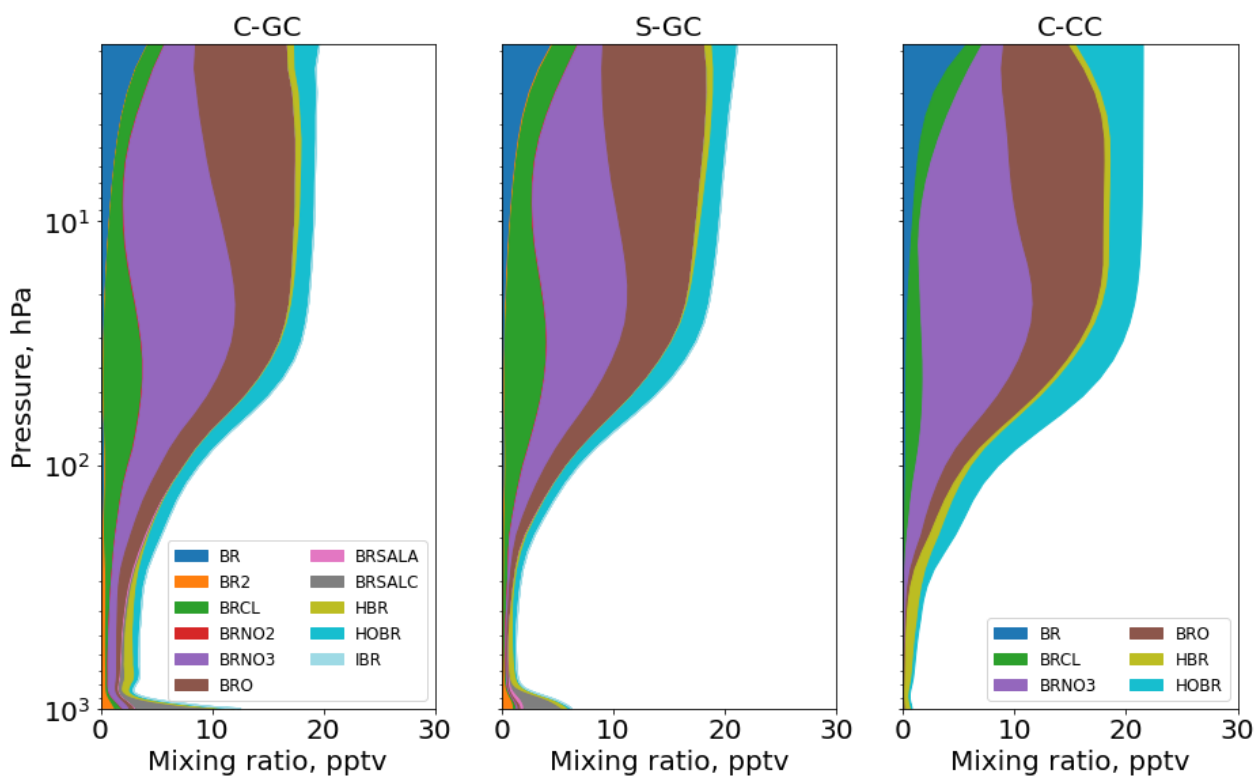
Figure 15. Global annual mean speciation of total organic and inorganic bromine as a function of altitude. Results are shown from C-GC (left), S-GC (middle), and C-CC (right), from the surface up to the model top (~2 hPa). Values correspond to the number of Br atoms present, such that (e.g.) the mixing ratio of Br_2 is multiplied by 2.

749   Br_y in the model stratosphere is dominated by the same species in all three configurations: BrO_x (Br + BrO), BrCl, $BrNO_3$,

750   HBr, and HOBr. The most significant difference is the greater proportion of HOBr in C-CC (~15%) than in S-GC or C-GC (8-

751   10%).

32

752

753   Between 30 hPa and the top of the boundary layer, the three models show divergent results. The only significant sources of

754   atmospheric Br_y in C-CC are CH_3Br, CH_2Br_2, and very long-lived bromine species such as halons which are insoluble. As a

755   result, tropospheric Br_y concentrations increase only slowly from the surface up to 300 hPa, at which point HOBr, BrO, and

756    $BrNO_3$ begin to form in significant quantities. In C-GC and S-GC, these sources of bromine are supplemented by bromine

757   from sea salt and surface Br_2 emissions. Mid-tropospheric Br_y concentrations are therefore largely set by the quantity of sea

758   salt bromine emitted, and by the fraction of that bromine which can be released to an insoluble form (e.g. Br_2) before the sea

759   salt is washed out of the atmosphere.

760

761   The greater concentration of mid-tropospheric Br_y in C-GC than in S-GC is likely due to differences in wet scavenging. Figure

762   16 shows the wet removal tendencies of bromine in fine sea salt (BrSALA) from large-scale and convective precipitation as

763   calculated by C-GC and S-GC. We find that there is greater wet deposition of fine sea salt bromine in S-GC than in C-GC,

764   despite removal rates below 900 hPa being greater in C-GC. Since total emissions of BrSALA are also 26% lower in S-GC

765   than in C-GC (Table 3), the slower mid-tropospheric mid-tropospheric removal of bromine in C-GC explains the greater

766   simulated concentration of Br_y in the mid troposphere.

767

768
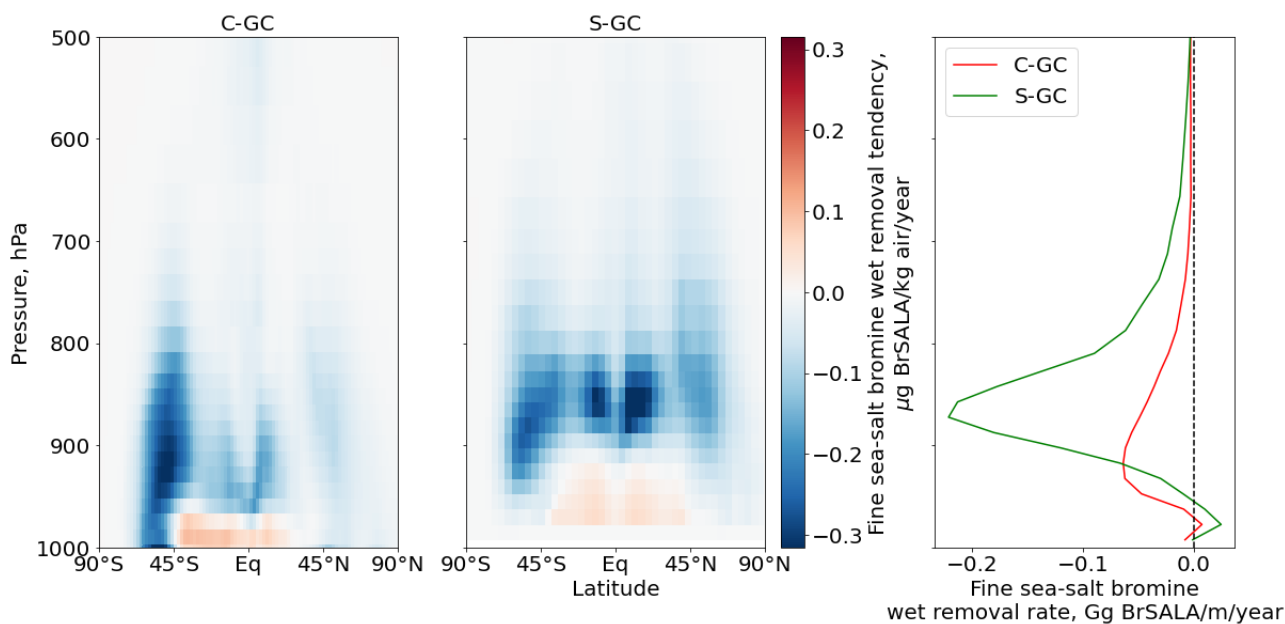
Figure 16. Zonal mean wet removal tendency of bromine carried in fine sea salt. Left and middle: Removal rates calculated by C-GC (left) and S-GC (middle). Right: Annual mean of fine sea salt bromine aerosol wet removal rate for C-GC (red), S-GC (green). Bromine in sea-salt aerosol is not modeled in CAM-chem.

772   C-GC also calculates wet deposition of non-MAM aerosols from both convective and large-scale precipitation independent of

773   convective transport, whereas S-GC calculates convective scavenging as part of convective transport. This means that soluble

774   species can be transported in convective updrafts in C-GC, unlike in S-GC.

775

3.2.4.3   Reactive chlorine (Cl_y)

We now focus on atmospheric chlorine by comparing its vertical profile and partitioning in all three models. Annually-averaged vertical profiles of reactive chlorine (Cl_y) are displayed in Figure 17, excluding source species such as chlorocarbons. A full list of the species used to define Cl_y in each configuration is provided in Figure 18.

As with total Br_y, total Cl_y has the same pattern of vertical distribution as S-GC up to around 10 hPa, but follows the pattern of C-CC above this point. The dominant factor in differences below 100 hPa is the lack of short-lived chlorine species such as sea salt in C-CC, which are the dominant source of chlorine to the lower troposphere. Above 10 hPa, the relative difference in Cl_y between C-GC and S-GC increases slowly from 2% at 10 hPa to 5% at 2 hPa, while the difference relative to C-CC remains at 19-20%.
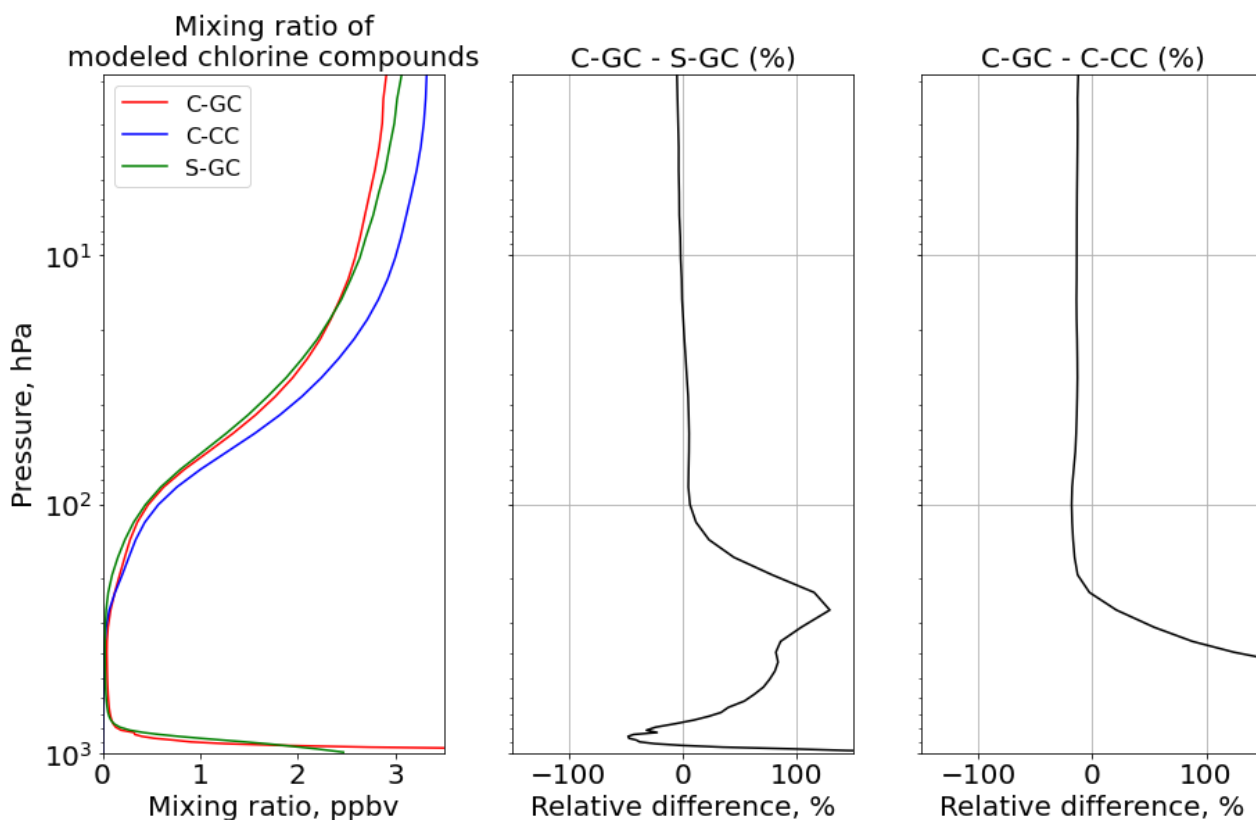
Figure 17. Comparison of annual average vertical profiles of chlorine-containing compounds in the three models. Left: Vertical profile of total gaseous chlorine mixing ratio for C-GC (red), S-GC (green), and C-CC (blue). Middle: Relative difference in Cl_y mixing ratio between C-GC and S-GC. Right: Relative difference in Cl_y mixing ratio between C-GC and C-CC. Although relative differences between C-GC and C-CC exceed 1000% near the surface, the limits on the rightmost panel are clipped to allow comparison to the center panel.

792 Figure 18 shows the speciation of Cl_y as a function of altitude in each model. The greater near-surface chlorine simulated by

793 C-GC and S-GC relative to C-CC is mostly made up of HCl and chlorine in sea salt (SALACL and SALCCL). In the

794 stratosphere there is no clear difference between partitioning in C-GC and S-GC. However, production of upper tropospheric

795 and lower stratospheric HCl and $ClNO_3$ from chlorine source compounds appears to occur faster and at lower altitudes in C-

796 CC. At 50 hPa total Cl_y in C-CC is 15% greater than in C-GC and S-GC, but the mean mixing ratio of HCl in C-CC is 45%

797 greater. Differences in $ClNO_3$ reach their peak at higher altitudes, around 20-30 hPa.

798
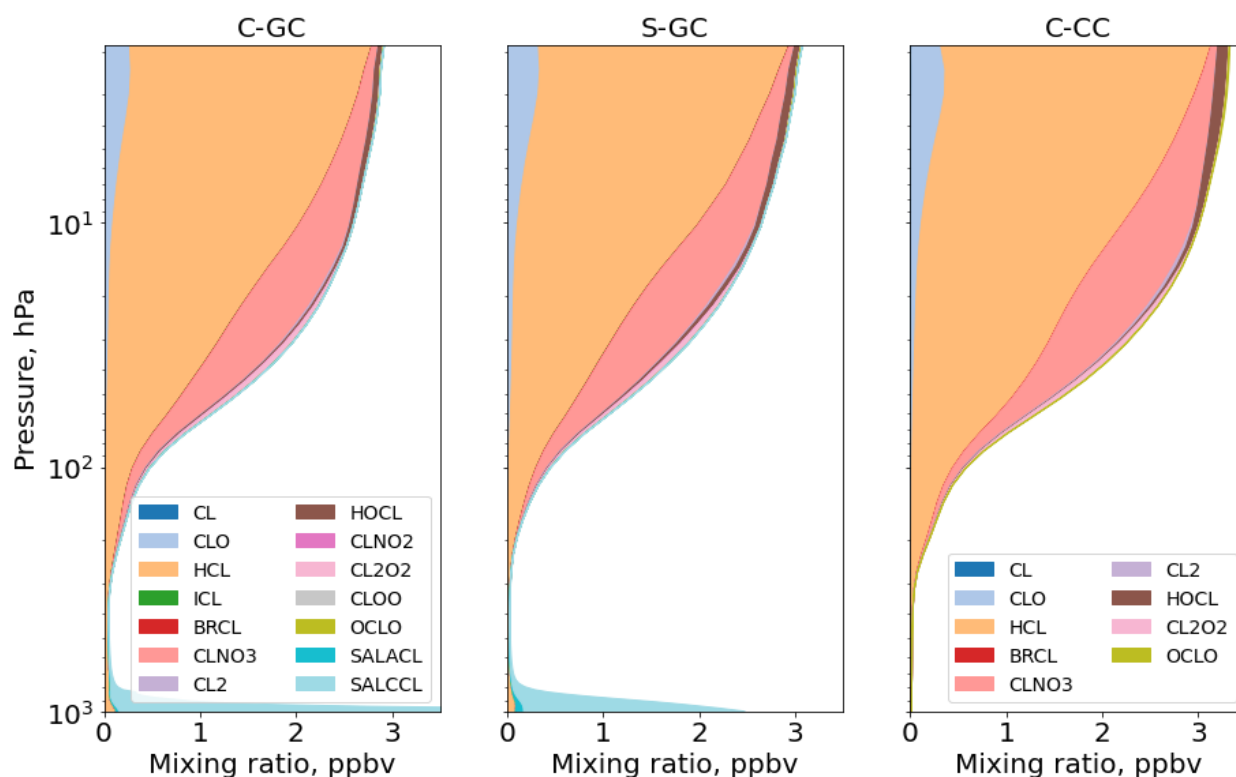
799

800 *Figure 18. Global annual mean vertical speciation of total organic and inorganic bromine in C-GC (left), S-GC (middle), and C-CC (right)*
801 *from the surface up to the model top (~2 hPa). Values correspond to the number of Cl atoms present, such that (e.g.) the mixing ratio of Cl2*
802 *is multiplied by 2. SALACL and SALCCL correspond to chlorine in fine and coarse sea salt, respectively.*

803 The global mean tropospheric concentration of Cl atoms is 590 cm^{-3}, roughly consistent with a recent evaluation from Wang

804 et al. (2021) which found a value of 630 cm^{-3}. This is 24% greater than the value from S-GC (477 cm^{-3}) and 160% greater than

805 that from C-CC (224 cm^{-3}), likely due to the greater emissions of sea salt and indicating that chlorine will play a greater role

806 in tropospheric oxidation in C-GC.

3.3 Comparison of model results to observations

We now compare the results from C-GC to observational data, with results from S-GC and C-CC also provided as context. Section 3.3.1 evaluates model performance at the surface, comparing to ground measurements of surface NO_2 and ozone. Section 3.3.2 compares model results to a climatology of vertical profiles of ozone, based on ozone sonde data. Section 3.3.3 evaluates the level of agreement of simulated ozone and carbon monoxide columns to measurements from the OMI/MLS and MOPITT satellite instruments. Finally, Section 3.3.4 evaluates the model against measurements of dry deposition fluxes and rainwater composition measurements.

3.3.1 Surface NO_2 and ozone

Figure 19 compares surface mass concentrations of NO_2 as estimated by C-GC, S-GC, and C-CC for 2016 against ground station measurements for North America, Europe, and South-East Asia (AirNow API, 2021; Environmental Numerical Database, 2021; China Air Quality Historical Data, 2021; European Air Quality Portal, 2021). All ground station measurements are the average value over 2016.

All three model configurations calculate lower mixing ratios than are reported by the ground observations. This is likely to be in part due to the presence of interferants such as HNO_3, which cause in-situ monitors to overestimate the concentration of NO_2 (Dunlea et al., 2007). However, S-GC is consistently biased lower than C-GC or C-CC. We also find that the surface NO_2 concentrations display variable agreement depending on the geographical location. In the U.S., Europe and South-East Asia, the correlation coefficient equals 0.39, 0.21 and 0.42 respectively for C-GC, similar to the results of 0.38, 0.21, and 0.41 from C-CC. S-GC provides correlation coefficients of 0.36, 0.21, and 0.41 respectively. This is expected given that the three model configurations all use the same input wind fields and NO_x emissions datasets. Nonetheless, both C-GC and C-CC estimate higher concentrations of NO_2 in northern China, northern Europe, and the northeast US than S-GC. This suggests that the representation of meteorology, photolysis, and NO_y removal processes have a greater impact on simulated NO_2 than the chemistry module alone.

830

831
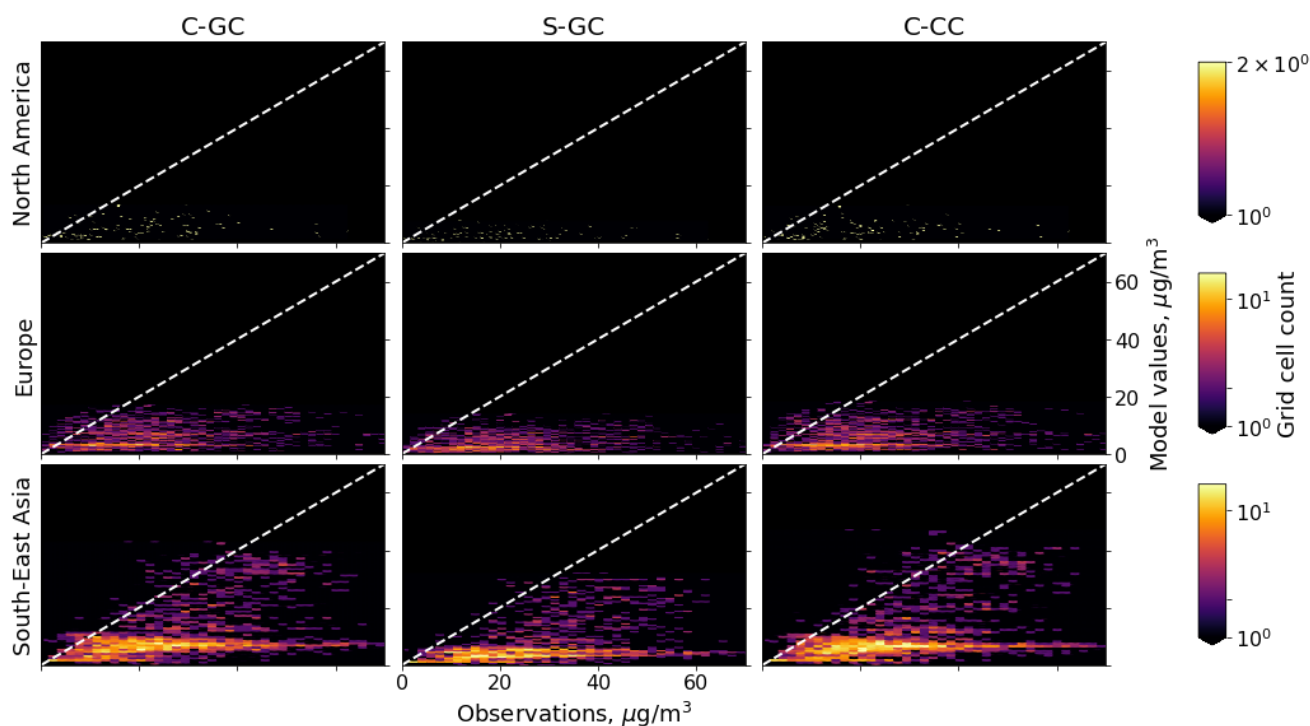
Figure 19. Annual average surface NO₂ mass concentrations simulated by C-GC (left), S-GC (middle), and C-CC (right) for 2016 compared against monitor measurements in North America (top), Europe (middle), and South East Asia (bottom).

834   Figure 20 shows the global distribution of NO_2, NO_x ($NO + NO_2$), and the ratio of annual mean NO to annual mean NO_2, and

835   thus provides some insight into possible causes of these disagreements. All three configurations show enhanced $NO:NO_2$ ratios

836   in polluted regions such as eastern China and over icy regions such as Greenland and Antarctica. However, S-GC shows

837   reduced $NO:NO_2$ ratios over land compared to either C-CC or C-GC. For example, ratios over North America in S-GC range

838   from 0.1 to 0.2, compared to a range of 0.01 to 0.1 in C-GC and C-CC. Surface $NO:NO_2$ ratios are typically dictated by surface

839   ozone and the NO_2 photolysis rate (Seinfeld and Pandis, 2006). Given that surface ozone concentrations in S-GC are typically

840   between those calculated in C-GC and C-CC (see Figure 21) and that S-GC and C-GC share the same photolysis treatment,

841   this discrepancy may instead be caused by the differences in cloudiness calculated by CESM compared to the MERRA-2 fields

842   read in by S-GC.

843
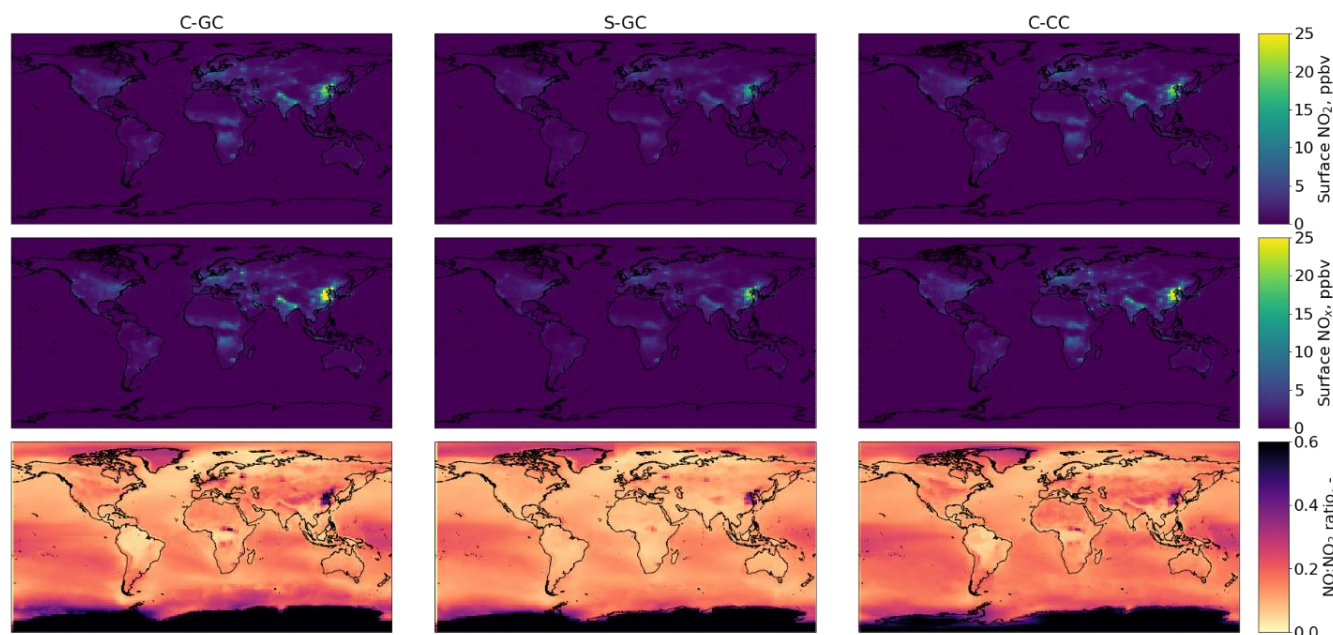
Figure 20. Surface-level NO$_2$, NO$_x$, and NO:NO$_2$ estimated by C-GC (left), S-GC (middle), and C-CC (right) for 2016. Top: annual average NO$_2$ in ppbv. Middle: annual average NO$_x$ (NO + NO$_2$) in ppbv. Bottom: annual average NO:NO$_2$, calculated as annual mean NO divided by annual mean NO$_2$ due to limited data availability.

847 Differences in NO:NO$_2$ may also be related to differences in emissions and treatment of oxidants such as VOCs and bromine.

848 C-GC and C-CC show a reduction in NO:NO$_2$ over the Amazon and in the Congo river basin, but this pattern is not reproduced

849 in S-GC. Similarly, topographical features including the Andes and Himalayas are visible in the C-CC and C-GC NO:NO$_2$

850 ratios, but not in the S-GC data – whereas a large reduction in NO:NO$_2$ over the Arctic Ocean is more pronounced in S-GC

851 and C-GC than in C-CC. This latter feature may be related to differences in the response of the simulated atmosphere to

852 anthropogenic emissions, as ship tracks are more visible in the C-GC and S-GC NO:NO$_2$ ratios (see e.g. Cape Horn and the

853 Cape of Good Hope) than in C-CC.

854

855 Figure 21 compares surface ozone against monitor measurements. The correlation coefficient between the model simulation

856 results over the U.S. and Europe and the surface measurements for surface ozone is 0.37 and 0.44 respectively. C-CC and S-

857 GC predict correlation coefficients of 0.24 and 0.44, and 0.28 and 0.43 respectively, indicating a potential improvement in

858 correlation in the U.S. but not Europe. The geographical pattern is also consistent, with high surface ozone concentrations over

859 the Mediterranean sea and lower concentrations over Northern Europe.

860

861 However, the results from all models appear to be biased low. As discussed in Section 3.2.2, C-GC estimates surface ozone

862 mixing ratios lower than either S-GC and C-CC, and therefore exhibits the greatest mean bias. C-GC, C-CC, and S-GC show

863 mean biases of -15, -9, and -10 ppbv for over Europe; -10, -3, and -5 ppbv over North America; and -20, -11, and -12 ppbv

864 over South-East Asia.

865
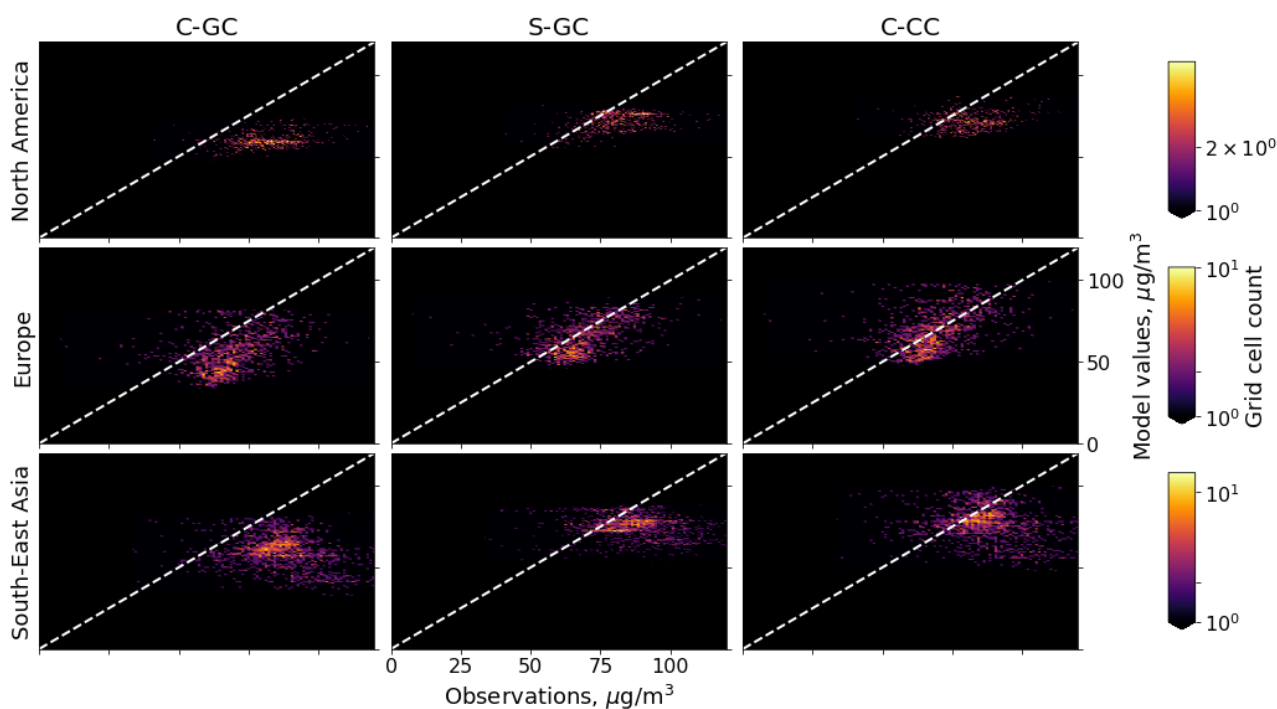
867 *Figure 21. Annual average surface ozone mass concentrations simulated by C-GC (left), S-GC (middle), and C-CC (right) for 2016*
868 *compared against monitor measurements in North America (top), Europe (middle), and South East Asia (bottom).*

869 The greater negative bias in simulated ozone shown by C-GC is likely related to both the different representation of

870 meteorology compared to S-GC and the greater bromine emissions compared to both S-GC and C-CC. However, further work

871 is needed to disentangle the root causes of discrepancies between the three models, and the common biases relative to

872 observations.

873 **3.3.2 Vertical profiles of ozone**

874 We now focus on the evaluation of the vertical profile of ozone mixing ratios by comparing C-GC, C-CC, and S-GC to a

875 climatology of ozone sonde observations from 1995-2010 (Tilmes et al., 2012). Over the past decades, observations from

876 ozone sondes in different locations provide a valuable dataset of the evolution of ozone mixing ratios in the troposphere and

877 stratosphere. Figure 22 provides a Taylor diagram comparison between the C-GC, C-CC, and S-GC simulations of 2016 to the
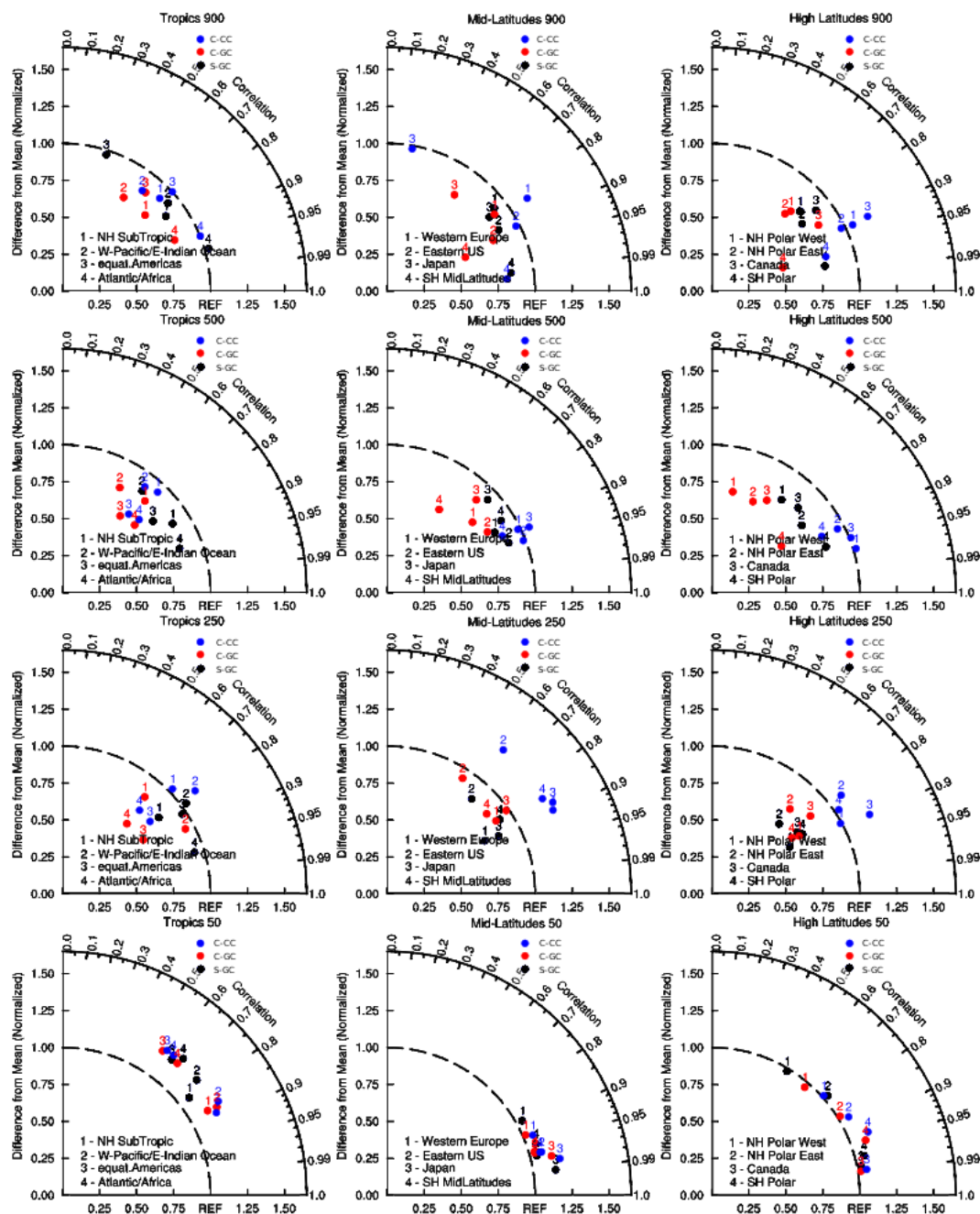
878 climatology.

879

880 In general, C-GC does not perform significantly better or worse than C-CC or S-GC, producing mean biases and correlations

881 in each region/altitude combination which are within the same range. The clearest exception is at low altitudes (900 or 500

882 hPa) and mid- to high latitudes. In these regions, C-GC results frequently show a smaller normalized difference from the mean

883 (radius) than either S-GC or C-CC, but also a weaker correlation with the observed seasonal cycle. The C-GC simulation of

884 tropical ozone also shows the smallest mean bias at all altitudes at or below 250 hPa, although again showing a weaker

885 correlation.

886

887 At high altitude (50 hPa), all three models appear to perform similarly. This may however simply reflect the lack of spin up

888 time. Since the three models only simulated two years in total, the simulated stratosphere will not have had time to fully

889 respond to the new model configuration. Longer simulations are needed to fully evaluate the performance and capability of

890 the C-GC stratosphere.

Figure 22. Taylor diagrams of the comparison of C-GC (red), C-CC (blue), and S-GC (black) simulations to a present-day (1995-2010) ozone sonde climatology. Top row to bottom row: comparisons at 900, 500, 250 and 50 hPa. Left column to right column: tropics, mid latitudes, and high latitudes. The normalized mean difference between simulations and observations for each region is shown on the radius, and the correlation of the seasonal cycle is shown as the angle from the vertical.

3.3.3 Total column ozone and CO

Figure 23 shows the annual mean total ozone column, expressed in Dobson Units, as measured by the Aura Ozone Monitoring Instrument (OMI) and Microwave Limb Sounder (MLS). The results from the satellite observations are compared to results from C-GC, C-CC, and S-GC. We find that on average the results from C-GC are 7.8 DU lower than the observations, mostly driven by an overestimation of stratospheric ozone depletion during the Antarctic spring of up to 16 DU. C-CC predicts a total ozone column that is 6.6 DU larger than the global mean ozone column. When broken down by tropospheric and stratospheric ozone column, we find that the bias in the stratospheric and tropospheric ozone columns for C-GC is -2 and -6 DU respectively, compared to +9.5 and -2.5 DU for C-CC. Additionally, we find that the bias in seasonal variations of total column ozone as predicted by C-GC range between -16 and -6 DU, while the variations range from -3 to +7 DU for C-CC. The model results from S-GC predict similar geographical biases in total ozone column as C-GC, although with a smaller net bias of -3.3 DU.
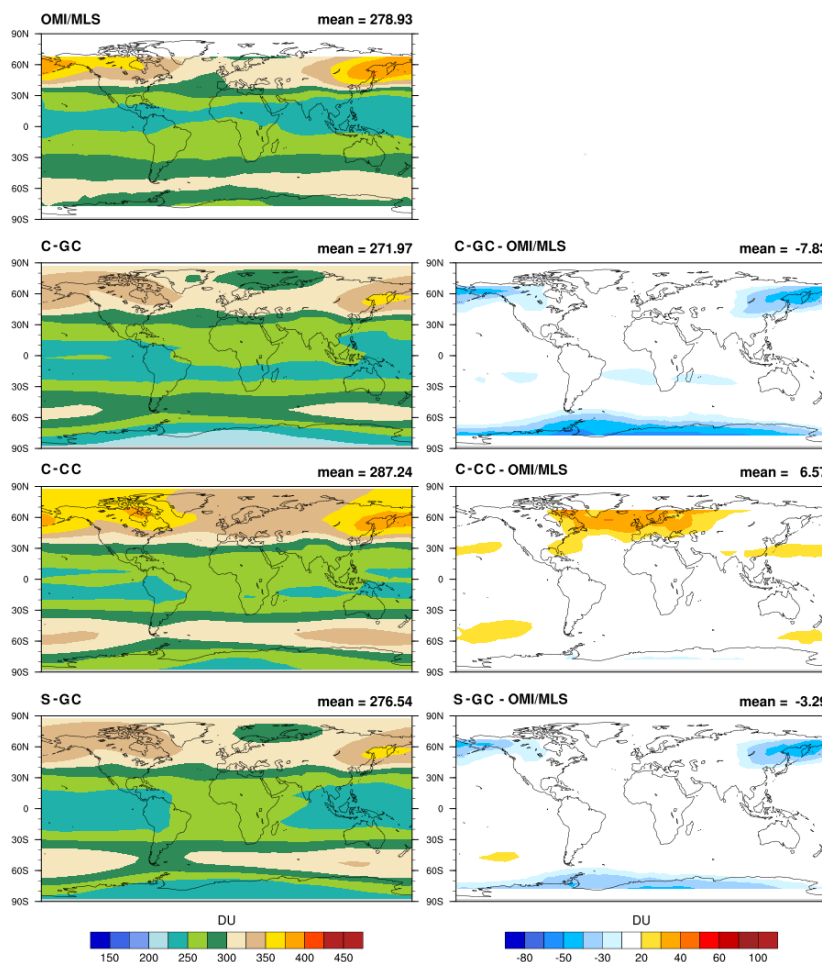

Figure 23. Total ozone column as observed by the Aura Ozone Monitoring Instrument (OMI) and Microwave Limb Sounder (MLS) for the 2004-2010 time period (1st row), compared to the results from C-GC (2nd row), C-CC (3rd row), and S-GC (4th row) for the year 2016. The measurements and model results are presented on the left, while the model biases are shown on the right.

912

913 Figure 24 compares the simulated total columns of carbon monoxide (CO) to retrievals from the MOPITT satellite instrument,

914 averaged for each April in the period 2003 to 2012. The model results as well as the model biases are shown for April 2016.

915 The CO model estimates using C-CC are characterized by a negative bias of -9×10^{17} molec/cm^2 in the Northern Hemisphere

916 that has been observed in previous model evaluations (Emmons et al., 2020). In C-GC, a negative bias still exists in the

917 Northern Hemisphere, but is smaller at -5×10^{17} molec/cm^2. Across all three model configurations a north-south gradient is

918 observed in the model bias, with the bias in the southern hemisphere being approximately 10^{18} molec/cm^2 more positive than

919 the (negative) bias in the northern hemisphere. The results from S-GC are nearly identical to those in C-GC, with a smaller

920 negative bias in the northern hemisphere than C-CC, but a larger positive bias in the southern hemisphere.

921
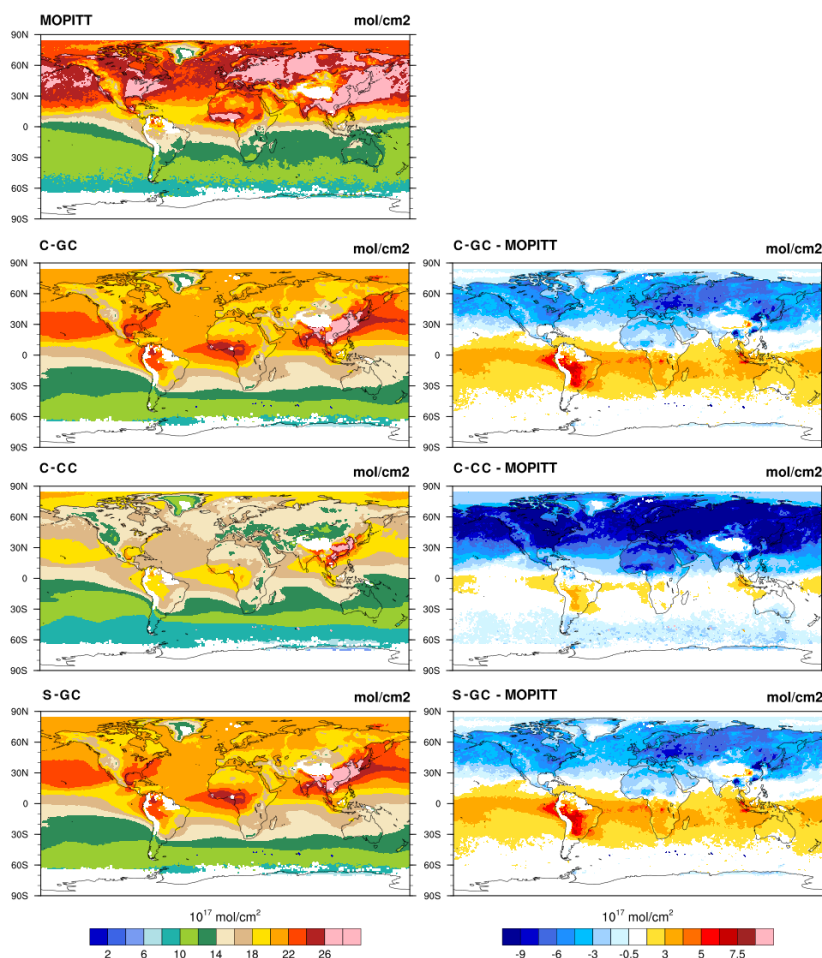
922
923 *Figure 24. Total carbon monoxide column during April, averaged from 2003 to 2012 and expressed in molecules per cm^2. The first row*
924 *displays the satellite observations from MOPITT. The simulation results and biases are presented for C-GC (2nd row), C-CC (3rd row), and*
925 *S-GC (4th row). The model evaluations are shown for April 2016.*

43

926 **3.3.4   Wet and dry deposition tendencies**

927   Finally, we compare simulated and observed surface deposition. Since deposition is the primary removal mechanism for

928   atmospheric reactive nitrogen and sulfur species, the ability of a model to reproduce observed patterns of deposition provides

929   an aggregate diagnostic for its representation of emissions, atmospheric chemistry, and the physical deposition processes.

930

931   Recent measurements have provided wet deposition rates in numerous geographical locations for the years 2005 to 2007 (Vet

932   et al., 2014). Dry deposition fluxes are available from the same study but are limited to sulfur and nitrogen species. They are

933   also limited to fewer geographical locations. Nonetheless we compare results from all three model configurations to the results

934   from Vet et al. below.

935

936   Figure 25 compares the model-evaluated wet deposition rates of nitrogen at the surface for C-GC, C-CC, and S-GC. The total

937   nitrogen flux is calculated by adding surface fluxes from each individual nitrogen compound undergoing wet deposition.

938   Rainwater composition measurements are also displayed where available for comparison. We find correlation coefficients of

939   0.65, 0.66, and 0.67 for C-GC, C-CC and S-GC respectively with these observations. On average, the results from C-GC are

940   closest to parity with a slope of 0.6, compared to 0.5 and 0.49 for C-CC and S-GC. We do not find any clear trends by location

941   between the three models.

942

943   Comparing the dry deposition flux of nitrogen species at the surface from C-GC, C-CC and S-GC to in-situ measurements

944   over North America from 2005 to 2007 shows that all models have positive biases. Relative to an observational mean of

945   1.57 kgN/ha/yr, C-GC has the best performance with a mean bias of +0.94 kgN/ha/yr, compared to +1.76 and +2.32 kgN/ha/yr

946   from S-GC and C-CC respectively. These biases from all three models can be explained by either larger concentrations of

947   nitrogen compounds or enhanced dry deposition velocities. However, we do not compensate for changes in nitrogen emissions

948   between the time of the observations (2005-2007) and the simulated period, during which NO_x emissions are estimated to have

949   increased (Emmons et al., 2020).
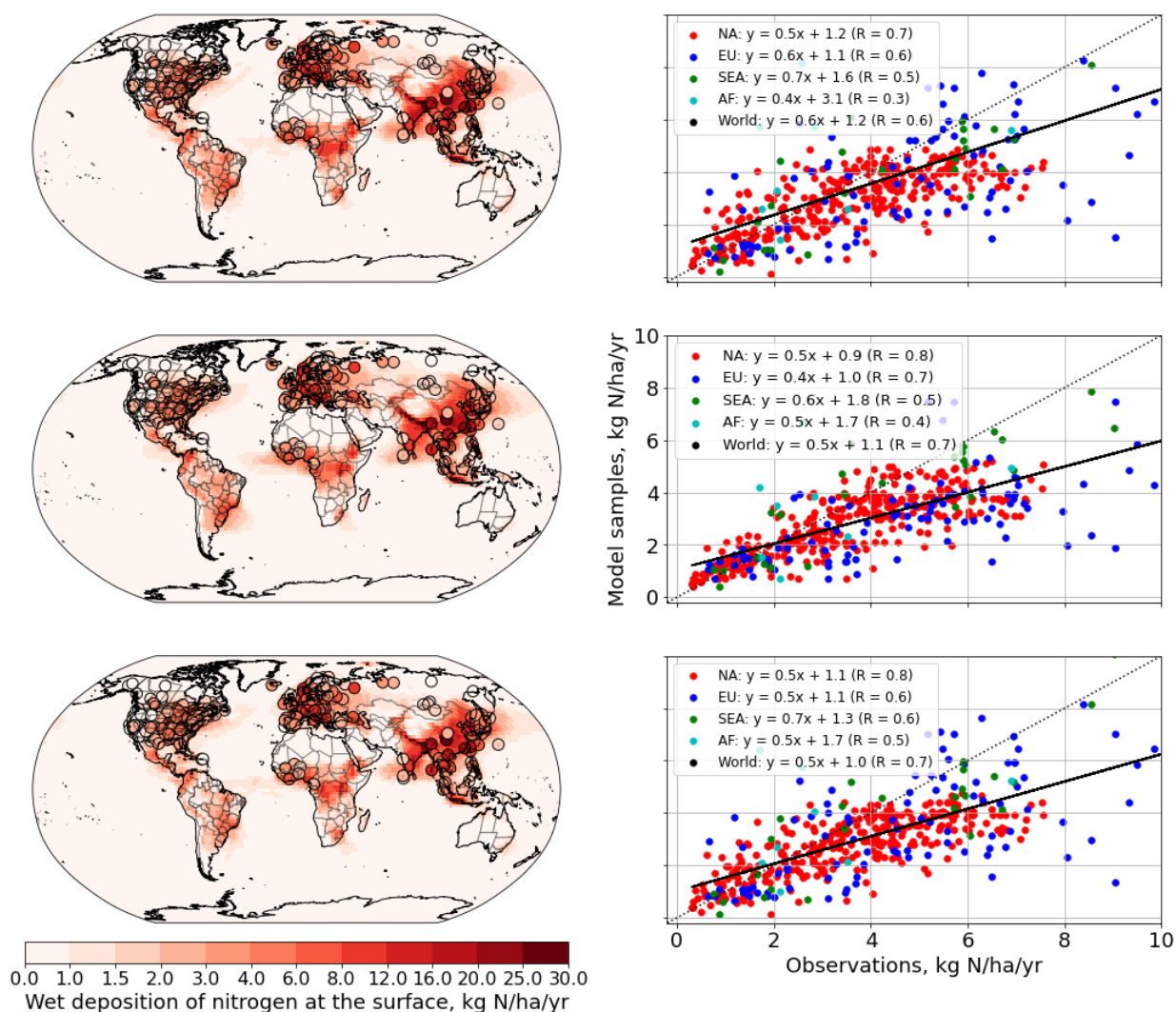
Figure 25. Geographical distribution of the wet deposition flux of nitrogen for C-GC (top), S-GC (middle), and C-CC (bottom). The annual mean value is shown as a map for each model, with circles used to indicate observational measurements (left). A parity plot of the results against the rainwater composition measurements is also provided for each model simulation (right).

Figure 26 displays the evaluated wet deposition rates of non-sea salt sulfur from C-GC, C-CC, and S-GC alongside measurements of sulfur in rainwater for 2005. When comparing across model results, we find a global mean deposition rate of 0.58, 0.38, and 0.50 kg S/ha/year in C-GC, S-GC, and C-CC respectively. The results from C-GC and C-CC show a correlation coefficient greater than 0.95, whereas C-GC and S-GC results show a correlation coefficient of 0.88.

Comparing to observational data, we find a mean bias of –2.40 kg S/ha/year (C-CC and C-GC) and –2.76 kg S/ha/year (S-GC) between the simulation results and rainwater composition measurements. This bias is location-dependent, with simulated data

45

962 for Asia showing a lower bias than North America or Europe. For instance, over North America, measurements indicate a

963 mean sulfur wet deposition flux of ~5 kg S/ha/year (for the year 2005), while the results from all three models at the same

964 stations reach a maximum of 1.5 kg S/ha/year (for the year 2016). This can be explained by the reduction in the sulfur wet

965 deposition surface flux over the past decades. Previous literature has found that the deposition rate of sulfur over the Eastern

966 U.S. has been decreasing at a rate of 1 kg S/ha/year[2] since 1990, with 60% of the reduction being in wet deposition rates and

967 40% in dry deposition rates (Zhang et al., 2018). Similar findings have been suggested for wet deposition rates over Europe

968 (Theobald et al., 2019). A similar, but more recent, decrease over Asia has also been observed (Aas et al., 2019).
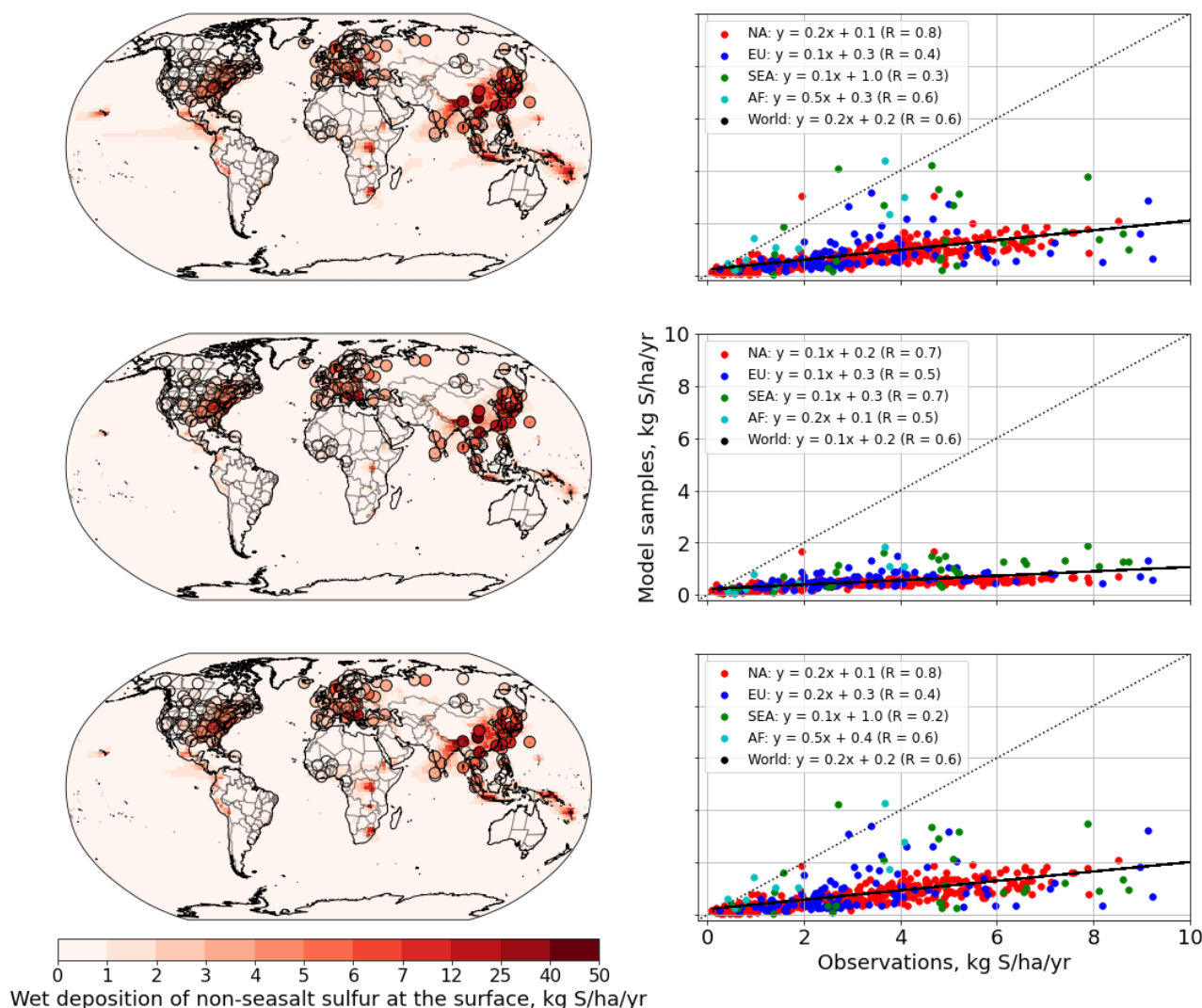
969

970

971 *Figure 26. As in Figure 25, but now for non-sea salt sulfur. Rows: C-GC (top), S-GC (middle), and C-CC (bottom).*

972 It is difficult to say with confidence that the calculated bias is purely due to lack of recent data without new measurements to

973 support this conclusion. However, our results do show that the simulation of sulfur deposition in C-GC more closely follows

974 that in C-CC than that in S-GC. This could be due to either the simulated distribution of precipitation, the representation of

975 aerosol, or the representation of scavenging processes, all of which differ between C-GC (or C-CC) and S-GC.

976 **4   Discussion and conclusion**

977 We present the first implementation of the GEOS-Chem chemistry mechanism as an option in the Community Earth System

978 Model (CESM). In addition to allowing users of CESM to take advantage of advancements in atmospheric modeling

979 implemented into the GEOS-Chem model, this also allows the community to better understand why models disagree and how

980 progress might be made to improve model performance and accuracy.

981

982 Our results suggest that differences in the representation of tropospheric halogen chemistry – in particular the representation

983 and magnitude of emissions of short-lived bromine and chlorine sources – may be responsible for differences in simulated

984 ozone between these model configurations. However, in addition to the recognized differences in chemical mechanisms, subtle

985 structural differences in atmospheric models may have a significant role. Our evaluation of tropospheric ozone concentrations

986 suggests that one of the key drivers in differences between CAM-chem and GEOS-Chem ozone fields differences may be

987 differences in free tropospheric water vapor. Similarly, we show that sulfur deposition rates are approximately twice as great

988 when running GEOS-Chem in a standalone model as opposed to running GEOS-Chem embedded in CESM, despite the use

989 of identical emissions.

990

991 We also find that differences in the representation of wet scavenging are a significant contributor to differences in reactive

992 nitrogen and halogen species distributions between GEOS-Chem and CAM-chem. The unification of convective transport and

993 scavenging in GEOS-Chem helps to prevent movement of soluble species to the upper troposphere through convective

994 updrafts, and therefore limits the effect of near surface halogen emissions from sea salt on ozone at higher altitudes.

995

996 Our implementation of GEOS-Chem in CESM is now publicly available for use. We envision that this model can become a

997 powerful tool for research, forecast, and regulatory applications of global atmospheric chemistry, air quality, and climate

998 research. However, this is also an important step towards the Multiscale Infrastructure for Chemistry and Aerosols (MUSICA),

999 and thereof a truly modular Earth system model. By enabling us to fairly compare models down to individual processes, we

1000 can begin to understand precisely why different models perform better or worse in reproducing different measurements and

1001 accelerate our efforts to improve atmospheric modeling fidelity as a whole.

1002

1003 Finally, this work will foster collaboration between the GEOS-Chem and CESM-CAM-chem communities. GEOS-Chem is
1004 presently used for research by over 100 university groups worldwide, and CAM-chem similarly has numerous users and
1005 developers. The availability of GEOS-Chem as an option in CESM will stimulate broader interest in the GEOS-Chem
1006 community to use CESM, and in the CESM community to use GEOS-Chem. Indeed, we expect that on-line simulation of
1007 atmospheric chemistry will become increasingly attractive to GEOS-Chem users as the resolution of dynamical models
1008 increase, and that CESM will provide the principal vehicle for this because of its public availability and support. By enabling
1009 improvements developed for GEOS-Chem to percolate into CESM without the need for re-implementation, this work will
1010 accelerate progress in atmospheric chemistry and Earth system modeling.

Author contributions

1012 TMF, SDE, HL, and EWL were responsible for the software development. TMF performed the investigation, formal analysis,
1013 and validation. SDE, LKE, SRHB, and DJJ conceived of the project and acquired funding. SDE, LKE, SG, SRHB, and DJJ
1014 supervised the work. TMF performed all visualization and prepared the original draft. Review and editing was performed by
1015 all co-authors. All contributions are defined according to the CRediT taxonomy (https://casrai.org/credit).

Acknowledgements

Code availability statement

1024 GEOS-Chem as an option within CESM is currently being implemented into the CESM main branch, such that no additional
1025 download will be needed to use it. However, a standalone copy of the specific implementation of CESM including GEOS-
1026 Chem which was used to generate the results in this manuscript is permanently archived at https://github.com/CESM-
1027 GC/CESM-GC-Standalone/releases/tag/v1.0.0_review (permanent DOI: https://doi.org/10.5281/zenodo.6465076). To
1028 reproduce the results of this work, the repository should be used as-is without using features such as checkout_externals to
1029 acquire any additional code.

1030 **Competing interests**

1031 The authors declare that they have no conflict of interest.

1032 **References**

1033 Aas, W., Mortier, A., Bowersox, V., Cherian, R., Faluvegi, G., Fagerli, H., Hand, J., Klimont, Z., Galy-Lacaux, C., Lehmann, C. M. B.,
1034 Myhre, C. L., Myhre, G., Olivié, D., Sato, K., Quaas, J., Rao, P. S. P., Schulz, M., Shindell, D., Skeie, R. B., Stein, A., Takemura, T.,
1035 Tsyro, S., Vet, R., and Xu, X.: Global and regional trends of atmospheric sulfur, Sci. Rep., 9, 953, 2019.

1036 Alexander, B., Park, R. J., Jacob, D. J., Li, Q. B., Yantosca, R. M., Savarino, J., Lee, C. C. W., and Thiemens, M. H.: Sulfate formation in
1037 sea-salt aerosols: Constraints from oxygen isotopes, J. Geophys. Res. D: Atmos., 110, 1–12, 2005.

1038 Amos, H. M., Jacob, D. J., Holmes, C. D., Fisher, J. A., Wang, Q., Yantosca, R. M., Corbitt, E. S., Galarneau, E., Rutter, A. P., Gustin, M.
1039 S., Steffen, A., Schauer, J. J., Graydon, J. A., Louis, V. L. S., Talbot, R. W., Edgerton, E. S., Zhang, Y., and Sunderland, E. M.: Gas-
1040 particle partitioning of atmospheric Hg(II) and its effect on global mercury deposition, Atmos. Chem. Phys., 12, 591–603, 2012.

1041 Andres, R. J. and Kasgnoc, A. D.: A time-averaged inventory of subaerial volcanic sulfur emissions, J. Geophys. Res., 103, 25251–25261,
1042 1998.

1043 AirNow API: https://docs.airnowapi.org/, last access: 9 September 2021.

1044 Badia, A., Iglesias-Suarez, F., Fernandez, R. P., Cuevas, C. A., Kinnison, D. E., Lamarque, J.-F., Griffiths, P. T., Tarasick, D. W., Liu, J.,
1045 and Saiz-Lopez, A.: The role of natural halogens in global tropospheric ozone chemistry and budget under different 21st century climate
1046 scenarios, J. Geophys. Res., 126, https://doi.org/10.1029/2021jd034859, 2021.

1047 Bey, I., Jacob, D. J., Yantosca, R. M., Logan, J. A., Field, B. D., Fiore, A. M., Li, Q., Liu, H. Y., Mickley, L. J., and Schultz, M. G.:
1048 Global modeling of tropospheric chemistry with assimilated meteorology: Model description and evaluation, J. Geophys. Res., 106,
1049 23073–23095, 2001.

1050 Bretherton, C., Balaji, V., Delworth, T., Dickinson, R. E., Edmonds, J. A., Famiglietti, J. S., and Smarr, L. L.: A national strategy for
1051 advancing climate modeling, National Academies Press, 2012.

1052 Carn, S. A., Yang, K., Prata, A. J., and Krotkov, N. A.: Extending the long-term record of volcanic SO_2 emissions with the Ozone
1053 Mapping and Profiler Suite nadir mapper: OMPS volcanic SO_2 measurements, Geophys. Res. Lett., 42, 925–932, 2015.

1054 China Air Quality Historical Data: https://quotsoft.net/air/, last access: 2021.

1055 Cohen, R. C. and Murphy, J. G.: Photochemistry of NO_2 in Earth's stratosphere: constraints from observations, Chem. Rev., 103, 4985–
1056 4998, 2003.

1057 Damian, V., Sandu, A., Damian, M., Potra, F., and Carmichael, G. R.: The kinetic preprocessor KPP-a software environment for solving
1058 chemical kinetics, Comput. Chem. Eng., 26, 1567–1579, 2002.

1059 Dunlea, E. J., Herndon, S. C., Nelson, D. D., Volkamer, R. M., San Martini, F., Sheehy, P. M., Zahniser, M. S., Shorter, J. H., Wormhoudt,
1060 J. C., Lamb, B. K., Allwine, E. J., Gaffney, J. S., Marley, N. A., Grutter, M., Marquez, C., Blanco, S., Cardenas, B., Retama, A., Ramos
1061 Villegas, C. R., Kolb, C. E., Molina, L. T., and Molina, M. J.: Evaluation of nitrogen dioxide chemiluminescence monitors in a polluted
1062 urban environment, Atmos. Chem. Phys., 7, 2691–2704, 2007.

1063 Eastham, S. D., Weisenstein, D. K., and Barrett, S. R. H.: Development and evaluation of the unified tropospheric–stratospheric chemistry
1064 extension (UCX) for the global chemistry-transport model GEOS-Chem, Atmos. Environ., 89, 52–63, 2014.

1065 Eastham, S. D., Long, M. S., Keller, C. A., Lundgren, E., Yantosca, R. M., Zhuang, J., Li, C., Lee, C. J., Yannetti, M., Auer, B. M., Clune,
1066 T. L., Kouatchou, J., Putman, W. M., Thompson, M. A., Trayanov, A. L., Molod, A. M., Martin, R. V., and Jacob, D. J.: GEOS-Chem
1067 High Performance (GCHP v11-02c): A next-generation implementation of the GEOS-Chem chemical transport model for massively

1068 parallel applications, Geosci. Model Dev., 2941–2953, 2018.

1069 Emmons, L. K., Arnold, S. R., Monks, S. A., Huijnen, V., Tilmes, S., Law, K. S., Thomas, J. L., Raut, J.-C., Bouarar, I., Turquety, S.,
1070 Long, Y., Duncan, B., Steenrod, S., Strode, S., Flemming, J., Mao, J., Langner, J., Thompson, A. M., Tarasick, D., Apel, E. C., Blake, D.
1071 R., Cohen, R. C., Dibb, J., Diskin, G. S., Fried, A., Hall, S. R., Huey, L. G., Weinheimer, A. J., Wisthaler, A., Mikoviny, T., Nowak, J.,
1072 Peischl, J., Roberts, J. M., Ryerson, T., Warneke, C., and Helmig, D.: The POLARCAT Model Intercomparison Project (POLMIP):
1073 overview and evaluation with observations, Atmos. Chem. Phys., 15, 6721–6744, 2015.

1074 Emmons, L. K., Schwantes, R. H., Orlando, J. J., Tyndall, G., Kinnison, D., Lamarque, J.-F., Marsh, D., Mills, M. J., Tilmes, S., Bardeen,
1075 C., Buchholz, R. R., Conley, A., Gettelman, A., Garcia, R., Simpson, I., Blake, D. R., Meinardi, S., and Pétron, G.: The chemistry
1076 mechanism in the community earth system model version 2 (CESM2), J. Adv. Model. Earth Syst., 12, e2019MS001882, 2020.

1077 European Air Quality Portal: https://discomap.eea.europa.eu/map/fme/AirQualityExport.htm, last access: 2021.

1078 Fahey, D., Newman, P. A., Pyle, J. A., Safari, B., Chipperfield, M. P., Karoly, D., Kinnison, D. E., Ko, M., Santee, M., and Doherty, S. J.:
1079 Scientific assessment of ozone depletion: 2018, global ozone research and monitoring project-report no. 58, World Meteorological
1080 Organization, 2018.

1081 Fairlie, D. T., Jacob, D. J., and Park, R. J.: The impact of transpacific transport of mineral dust in the United States, Atmos. Environ., 41,
1082 1251–1266, 2007.

1083 Feng, X., Lin, H., Fu, T.-M., Sulprizio, M. P., Zhuang, J., Jacob, D. J., Tian, H., Ma, Y., Zhang, L., Wang, X., Chen, Q., and Han, Z.:
1084 WRF-GC (v2.0): online two-way coupling of WRF (v3.9.1.1) and GEOS-Chem (v12.7.2) for modeling regional atmospheric chemistry–
1085 meteorology interactions, Geosci. Model Dev., 14, 3741–3768, 2021.

1086 Fernandez, R. P., Barrera, J. A., López-Noreña, A. I., Kinnison, D. E., Nicely, J., Salawitch, R. J., Wales, P. A., Toselli, B. M., Tilmes, S.,
1087 Lamarque, J.-F., Cuevas, C. A., and Saiz-Lopez, A.: Intercomparison Between Surrogate, Explicit, and Full Treatments of VSL Bromine
1088 Chemistry Within the CAM-Chem Chemistry-Climate Model, Geophys. Res. Lett., 48, e2020GL091125, 2021.

1089 Fountoukis, C. and Nenes, A.: ISORROPIA II: a computationally efficient thermodynamic equilibrium model for K^+-Ca^{2+}-Mg^{2+}-NH_4-Na^+-
1090 SO_4^{2+}-NO_3^--Cl^--H_2O aerosols, 4639–4659, 2007.

1091 Ge, C., Wang, J., Carn, S., Yang, K., Ginoux, P., and Krotkov, N.: Satellite-based global volcanic SO_2 emissions and sulfate direct
1092 radiative forcing during 2005-2012, J. Geophys. Res., 121, 3446–3464, 2016.

1093 Guenther, a. B., Jiang, X., Heald, C. L., Sakulyanontvittaya, T., Duhl, T., Emmons, L. K., and Wang, X.: The model of emissions of gases
1094 and aerosols from nature version 2.1 (MEGAN2.1): An extended and updated framework for modeling biogenic emissions, 5, 1471–1492,
1095 2012.

1096 Hill, C., DeLuca, C., Balaji, Suarez, M., and Silva, A. D.: The architecture of the Earth System Modeling Framework, 6, 18–28, 2004.

1097 Hoesly, R. M., Smith, S. J., Feng, L., Klimont, Z., Janssens-Maenhout, G., Pitkanen, T., Seibert, J. J., Vu, L., Andres, R. J., Bolt, R. M.,
1098 Bond, T. C., Dawidowski, L., Kholod, N., Kurokawa, J.-I., Li, M., Liu, L., Lu, Z., Moura, M. C. P., O'Rourke, P. R., and Zhang, Q.:
1099 Historical (1750–2014) anthropogenic emissions of reactive gases and aerosols from the Community Emissions Data System (CEDS),
1100 Geoscientific Model Development, 11, 369–408, 2018.

1101 Hu, L., Keller, C. A., Long, M. S., Sherwen, T., Auer, B., Da Silva, A., Nielsen, J. E., Pawson, S., Thompson, M. A., Trayanov, A. L.,
1102 Travis, K. R., Grange, S. K., Evans, M. J., and Jacob, D. J.: Global simulation of tropospheric chemistry at 12.5 km resolution:
1103 performance and evaluation of the GEOS-Chem chemical module (v10-1) within the NASA GEOS Earth system model (GEOS-5 ESM),
1104 Geosci. Model Dev., 11, 4603–4620, 2018.

1105 Hurrell, J. W., Holland, M. M., Gent, P. R., Ghan, S., Kay, J. E., Kushner, P. J., Lamarque, J.-F., Large, W. G., Lawrence, D., Lindsay, K.,
1106 Lipscomb, W. H., Long, M. C., Mahowald, N., Marsh, D. R., Neale, R. B., Rasch, P., Vavrus, S., Vertenstein, M., Bader, D., Collins, W.
1107 D., Hack, J. J., Kiehl, J., and Marshall, S.: The Community Earth System Model: A Framework for Collaborative Research, Bull. Am.
1108 Meteorol. Soc., 94, 1339–1360, 2013.

1109 Jaeglé, L., Quinn, P. K., Bates, T. S., Alexander, B., and Lin, J. T.: Global distribution of sea salt aerosols: New constraints from in situ
1110 and remote sensing observations, Atmos. Chem. Phys., 11, 3137–3157, 2011.

1111 Jaeglé, L., Shah, V., Thornton, J. A., Lopez-Hilfiker, F. D., Lee, B. H., McDuffie, E. E., Fibiger, D., Brown, S. S., Veres, P., Sparks, T. L.,
1112 Ebben, C. J., Wooldridge, P. J., Kenagy, H. S., Cohen, R. C., Weinheimer, A. J., Campos, T. L., Montzka, D. D., Digangi, J. P., Wolfe, G.
1113 M., Hanisco, T., Schroder, J. C., Campuzano-Jost, P., Day, D. A., Jimenez, J. L., Sullivan, A. P., Guo, H., and Weber, R. J.: Nitrogen
1114 oxides emissions, chemistry, deposition, and export over the northeast United States during the WINTER aircraft campaign, J. Geophys.
1115 Res., 123, 12,368-12,393, 2018.

1116 Environmental Numerical Database: https://www.nies.go.jp/igreen/index.html, last access: 2021.

1117 Jöckel, P., von Kuhlmann, R., Lawrence, M. G., Steil, B., Brenninkmeijer, C. A. M., Crutzen, P. J., Rasch, P. J., and Eaton, B.: On a
1118 fundamental problem in implementing flux-form advection schemes for tracer transport in 3-dimensional general circulation and chemistry
1119 transport models, Q.J.R. Meteorol. Soc., 127, 1035–1052, 2001.

1120 Jonson, J. E., Schulz, M., Emmons, L., Flemming, J., Henze, D., Sudo, K., Tronstad Lund, M., Lin, M., Benedictow, A., Koffi, B.,
1121 Dentener, F., Keating, T., Kivi, R., and Davila, Y.: The effects of intercontinental emission sources on European air pollution levels,
1122 Atmos. Chem. Phys., 18, 13655–13672, 2018.

1123 Keller, C., Auer, B., Hu, L., Jacob, D., Long, M., Nielsen, E., Pawson, S., da Silva, A., and Thompson, M.: High-resolution GEOS-5
1124 nature run with tropospheric chemistry, 2017.

1125 Keller, C. A., Long, M. S., Yantosca, R. M., Da Silva, A. M., Pawson, S., and Jacob, D. J.: HEMCO v1.0: a versatile, ESMF-compliant
1126 component for calculating emissions in atmospheric models, Geoscientific Model Development, 7, 1409–1417, 2014.

1127 Keller, C. A., Knowland, K. E., Duncan, B. N., Liu, J., Anderson, D. C., Das, S., Lucchesi, R. A., Lundgren, E. W., Nicely, J. M., Nielsen,
1128 E., Ott, L. E., Saunders, E., Strode, S. A., Wales, P. A., Jacob, D. J., and Pawson, S.: Description of the NASA GEOS composition forecast
1129 modeling system GEOS-CF v1.0, J. Adv. Model. Earth Syst., 13, https://doi.org/10.1029/2020ms002413, 2021.

1130 Kinnison, D. E., Brasseur, G. P., and Walters, S.: Sensitivity of chemical tracers to meteorological parameters in the MOZART-3 chemical
1131 transport model, 2007.

1132 Kodros, J. K. and Pierce, J. R.: Important global and regional differences in aerosol cloud-albedo effect estimates between simulations
1133 with and without prognostic aerosol microphysics, J. Geophys. Res., 122, 4003–4018, 2017.

1134 Lamarque, J.-F., Emmons, L. K., Hess, P. G., Kinnison, D. E., Tilmes, S., Vitt, F., Heald, C. L., Holland, E. a., Lauritzen, P. H., Neu, J.,
1135 Orlando, J. J., Rasch, P. J., and Tyndall, G. K.: CAM-chem: description and evaluation of interactive atmospheric chemistry in the
1136 Community Earth System Model, 5, 369–411, 2012.

1137 Lin, H., Feng, X., Fu, T.-M., Tian, H., Ma, Y., Zhang, L., Jacob, D. J., Yantosca, R. M., Sulprizio, M. P., Lundgren, E. W., and Others:
1138 WRF-GC (v1. 0): online coupling of WRF (v3. 9.1. 1) and GEOS-Chem (v12. 2.1) for regional atmospheric chemistry modeling--Part 1:
1139 Description of the one-way model, 13, 3241–3265, 2020.

1140 Lin, H., Jacob, D. J., Lundgren, E. W., Sulprizio, M. P., Keller, C. A., Fritz, T. M., Eastham, S. D., Emmons, L. K., Campbell, P. C.,
1141 Baker, B., Saylor, R. D., and Montuoro, R.: Harmonized Emissions Component (HEMCO) 3.0 as a versatile emissions component for
1142 atmospheric models: application in the GEOS-Chem, NASA GEOS, WRF-GC, CESM2, NOAA GEFS-Aerosol, and NOAA UFS models,
1143 2021.

1144 Liu, H., Jacob, D. J., Bey, I., and Yantosca, R. M.: Constraints from ^{210}Pb and ^{7}Be on wet deposition and transport in a global three-
1145 dimensional chemical tracer model driven by assimilated meteorological fields, J. Geophys. Res., 106, 12109–12128, 2001.

1146 Liu, X., Easter, R. C., Ghan, S. J., Zaveri, R., Rasch, P., Shi, X., Lamarque, J.-F., Gettelman, A., Morrison, H., Vitt, F., Conley, A., Park,
1147 S., Neale, R., Hannay, C., Ekman, A. M. L., Hess, P., Mahowald, N., Collins, W., Iacono, M. J., Bretherton, C. S., Flanner, M. G., and
1148 Mitchell, D.: Toward a minimal representation of aerosols in climate models: description and evaluation in the Community Atmosphere
1149 Model CAM5, Geosci. Model Dev., 5, 709–739, 2012.

1150 Liu, X., Ma, P.-L., Wang, H., Tilmes, S., Singh, B., Easter, R. C., Ghan, S. J., and Rasch, P. J.: Description and evaluation of a new four-
1151 mode version of the Modal Aerosol Module (MAM4) within version 5.3 of the Community Atmosphere Model, Geosci. Model Dev., 9,
1152 505–522, 2016.

1153 Long, M. S., Yantosca, R., Nielsen, J. E., Keller, C. A., da Silva, A., Sulprizio, M. P., Pawson, S., and Jacob, D. J.: Development of a grid-

independent GEOS-Chem chemical transport model (v9-02) as an atmospheric chemistry module for Earth system models, Geoscientific
Model Development, 8, 595–602, 2015.

Marais, E. A., Jacob, D. J., Jimenez, J. L., Campuzano-Jost, P., Day, D. A., Hu, W., Krechmer, J., Zhu, L., Kim, P. S., Miller, C. C., and
Others: Aqueous-phase mechanism for secondary organic aerosol formation from isoprene: application to the southeast United States and
co-benefit of SO 2 emission controls, Atmos. Chem. Phys., 16, 1603–1618, 2016.

Mills, M. J., Schmidt, A., Easter, R., Solomon, S., Kinnison, D. E., Ghan, S. J., Neely, R. R., III, Marsh, D. R., Conley, A., Bardeen, C. G.,
and Gettelman, A.: Global volcanic aerosol properties derived from emissions, 1990–2014, using CESM1(WACCM), J. Geophys. Res.,
121, 2332–2348, 2016.

Murray, L. T., Jacob, D. J., Logan, J. A., Hudman, R. C., and Koshak, W. J.: Optimized regional and interannual variability of lightning in
a global chemical transport model constrained by LIS/OTD satellite data, J. Geophys. Res., 117, D20307, 2012.

Neely, R. R., III and Schmidt, A.: VolcanEESM: Global volcanic sulphur dioxide (SO2) emissions database from 1850 to present,
https://doi.org/10.5285/76ebdc0b-0eed-4f70-b89e-55e606bcd568, 2016.

Neu, J. L. and Prather, M. J.: Toward a more physical representation of precipitation scavenging in global chemistry models: cloud overlap
and ice physics and their impact on tropospheric ozone, Atmos. Chem. Phys., 12, 3289–3310, 2012.

Nicely, J. M., Salawitch, R. J., Canty, T., Anderson, D. C., Arnold, S. R., Chipperfield, M. P., Emmons, L. K., Flemming, J., Huijnen, V.,
Kinnison, D. E., Lamarque, J.-F., Mao, J., Monks, S. A., Steenrod, S. D., Tilmes, S., and Turquety, S.: Quantifying the causes of
differences in tropospheric OH within global models, J. Geophys. Res., 122, 1983–2007, 2017.

NRC: The Future of Atmospheric Chemistry Research: Remembering Yesterday, Understanding Today, Anticipating Tomorrow,
{National Research Council}, 226 pp., 2016.

Park, R. J.: Natural and transboundary pollution influences on sulfate-nitrate-ammonium aerosols in the United States: Implications for
policy, J. Geophys. Res., 109, 13,791, 2004.

Park, R. J., Oak, Y. J., Emmons, L. K., Kim, C.-H., Pfister, G. G., Carmichael, G. R., Saide, P. E., Cho, S.-Y., Kim, S., Woo, J.-H.,
Crawford, J. H., Gaubert, B., Lee, H.-J., Park, S.-Y., Jo, Y.-J., Gao, M., Tang, B., Stanier, C. O., Shin, S. S., Park, H. Y., Bae, C., and Kim,
E.: Multi-model intercomparisons of air quality simulations for the KORUS-AQ campaign, Elementa: Science of the Anthropocene, 9,
https://doi.org/10.1525/elementa.2021.00139, 2021.

Pickering, K. E., Wang, Y., Tao, W.-K., Price, C., and Müller, J.-F.: Vertical distributions of lightning NO x for use in regional and global
chemical transport models, J. Geophys. Res., 103, 31203–31216, 1998.

Pound, R. J., Sherwen, T., Helmig, D., Carpenter, L. J., and Evans, M. J.: Influences of oceanic ozone deposition on tropospheric
photochemistry, Atmos. Chem. Phys., 20, 4227–4239, 2020.

Fast-JX v7.0a:

Price, C., Penner, J., and Prather, M.: NOx from lightning: 1. Global distribution based on lightning physics, J. Geophys. Res., 102, 5929–
5941, 1997.

Pye, H. O. T. and Seinfeld, J. H.: A global perspective on aerosol from low-volatility organic compounds, Atmos. Chem. Phys., 10, 4377–
4401, 2010.

Pye, H. O. T., Chan, A. W. H., Barkley, M. P., and Seinfeld, J. H.: Global modeling of organic aerosol: the importance of reactive nitrogen
(NOx and NO3), Atmos. Chem. Phys., 10, 11261–11276, 2010.

Sandgathe, S., O'Connor, W., Lett, N., McCarren, D., and Toepfer, F.: National Unified Operational Prediction Capability Initiative, Bull.
Am. Meteorol. Soc., 92, 1347–1351, 2011.

Seinfeld, J. H. and Pandis, S. N.: Atmospheric Chemistry and Physics, 2nd ed., Wiley, 2006.

Simone, N. W., Stettler, M. E. J., and Barrett, S. R. H.: Rapid estimation of global civil aviation emissions with uncertainty quantification,

Transp. Res. Part D: Trans. Environ., 25, 33–41, 2013.

Theobald, M. R., Vivanco, M. G., Aas, W., Andersson, C., Ciarelli, G., Couvidat, F., Cuvelier, K., Manders, A., Mircea, M., Pay, M.-T., and Others: An evaluation of European nitrogen and sulfur wet deposition and their trends estimated by six chemistry transport models for the period 1990--2010, Atmos. Chem. Phys., 19, 379–405, 2019.

Tilmes, S., Lamarque, J.-F., Emmons, L. K., Conley, A., Schultz, M. G., Saunois, M., Thouret, V., Thompson, A. M., Oltmans, S. J., Johnson, B., and Tarasick, D.: Technical Note: Ozonesonde climatology between 1995 and 2011: description, evaluation and applications, Atmos. Chem. Phys., 12, 7475–7497, 2012.

Tilmes, S., Lamarque, J.-F., Emmons, L. K., Kinnison, D. E., Marsh, D., Garcia, R. R., Smith, A. K., Neely, R. R., Conley, A., Vitt, F., Val Martin, M., Tanimoto, H., Simpson, I., Blake, D. R., and Blake, N.: Representation of the Community Earth System Model (CESM1) CAM4-chem within the Chemistry-Climate Model Initiative (CCMI), Geosci. Model Dev., 9, 1853–1890, 2016.

Tilmes, S., Hodzic, A., Emmons, L. K., Mills, M. J., Gettelman, A., Kinnison, D. E., Park, M., Lamarque, J.-F., Vitt, F., Shrivastava, M., Campuzano-Jost, P., Jimenez, J. L., and Liu, X.: Climate forcing and trends of organic aerosols in the community earth system model (CESM2), J. Adv. Model. Earth Syst., 11, 4323–4351, 2019.

Vet, R., Artz, R. S., Carou, S., Shaw, M., Ro, C.-U., Aas, W., Baker, A., Bowersox, V. C., Dentener, F., Galy-Lacaux, C., Hou, A., Pienaar, J. J., Gillett, R., Forti, M. C., Gromov, S., Hara, H., Khodzher, T., Mahowald, N. M., Nickovic, S., Rao, P. S. P., and Reid, N. W.: A global assessment of precipitation chemistry and deposition of sulfur, nitrogen, sea salt, base cations, organic acids, acidity and pH, and phosphorus, Atmos. Environ., 93, 3–100, 2014.

Vinken, G. C. M., Boersma, K. F., Jacob, D. J., and Meijer, E. W.: Accounting for non-linear chemistry of ship plumes in the GEOS-Chem global chemistry transport model, Atmos. Chem. Phys., 11, 11707–11722, 2011.

Wang, X., Jacob, D. J., Eastham, S. D., Sulprizio, M. P., Zhu, L., Chen, Q., Alexander, B., Sherwen, T., Evans, M. J., Lee, B. H., Haskins, J. D., Lopez-Hilfiker, F. D., Thornton, J. A., Huey, G. L., and Liao, H.: The role of chlorine in global tropospheric chemistry, Atmos. Chem. Phys., 19, 3981–4003, 2019.

Wang, X., Jacob, D. J., Downs, W., Zhai, S., Zhu, L., Shah, V., Holmes, C. D., Sherwen, T., Alexander, B., Evans, M. J., Eastham, S. D., Neuman, J. A., Veres, P., Koenig, T. K., Volkamer, R., Huey, L. G., Bannan, T. J., Percival, C. J., Lee, B. H., and Thornton, J. A.: Global tropospheric halogen (Cl, Br, I) chemistry and its impact on oxidants, Atmos. Chem. Phys., https://doi.org/10.5194/acp-2021-441, 2021.

Wang, Y., Jacob, D. J., and Logan, J. A.: Global simulation of tropospheric O_3-NO_x-hydrocarbon chemistry: 1. Model formulation, J. Geophys. Res., 103, 10713–10725, 1998.

Wesely, M.: Parameterization of Surface Resistances to Gaseous Dry Deposition in Regional-Scale Numerical-Models, 765 Atmos. Environ., 23, 1293-1304, 1989.

Wild, O., Zhu, X., and Prather, M. J.: Fast-J: Accurate simulation of in- and below-cloud photolysis in tropospheric chemical models, J. Atmos. Chem., 245–282, 2000.

Wu, S., Mickley, L. J., Jacob, D. J., Logan, J. A., Yantosca, R. M., and Rind, D.: Why are there large differences between models in global budgets of tropospheric ozone?, J. Geophys. Res., 112, D05302, 2007.

Yu, F. and Luo, G.: Simulation of particle size distribution with a global aerosol model: contribution of nucleation to aerosol and CCN number concentrations, Atmos. Chem. Phys., 9, 7691–7710, 2009.

Yu, K., Keller, C. A., Jacob, D. J., Molod, A. M., Eastham, S. D., and Long, M. S.: Errors and improvements in the use of archived meteorological data for chemical transport modeling: an analysis using GEOS-Chem v11-01 driven by GEOS-5 meteorology, Geoscientific Model Development, 11, 305–319, 2018.

Zender, C. S.: Mineral Dust Entrainment and Deposition (DEAD) model: Description and 1990s dust climatology, J. Geophys. Res., 108, https://doi.org/10.1029/2002jd002775, 2003.

Zhang, L., Gong, S., Padro, J., and Barrie, L.: A size-segregated particle dry deposition scheme for an atmospheric aerosol module, Atmos. Environ., 35, 549–560, 2001.

1236   Zhang, Y., Mathur, R., Bash, J. O., Hogrefe, C., Xing, J., and Roselle, S. J.: Long-term trends in total inorganic nitrogen and sulfur
1237   deposition in the US from 1990 to 2010, Atmos. Chem. Phys., 18, 9091–9106, 2018.